Equiaxed Dendritic Solidification with Convection: Part II. Numerical Simulations for an Al-4 Wt Pct Cu Alloy

C.Y. WANG and C. BECKERMANN

The multiphase model developed in part I for equiaxed dendritic solidification with melt convection and solid-phase transport is applied to numerically predict structural and compositional development in an Al-4 wt pct Cu alloy solidifying in a rectangular cavity. A numerical technique combining a fully implicit control-volume-based finite difference method with a multiple time-step scheme is developed for accurate and efficient simulations of both micro- and macroscale phenomena. Quantitative results for the dendritic microstructure evolution in the presence of melt convection and solid movement are obtained. The remarkable effects of the solid-liquid multiphase flow pattern on macrosegregation as well as the grain size distribution are illustrated.

I. INTRODUCTION

In recent years, numerical modeling of equiaxed dendritic solidification without convection has experienced considerable progress.[1,2] Nucleation and growth kinetic laws have been coupled with transient heat conduction calculations to determine the solidification microstructure. However, simulations of equiaxed dendritic solidification, taking melt convection and solid movement into account, have not been attempted in the literature, with the exception being the numerical study by Ni and Beckermann,[3] which includes both liquid convection and solid transport but deals with globulitic structures only (as opposed to dendritic).

This second article of the series describes a first attempt toward predicting equiaxed dendritic microstructures in the presence of melt convection and solid movement using the multiphase model developed by Wang and Beckermann[4] (hereinafter referred to as part I). The microstructural features of particular interest include the grain size and the internal solid fraction, which is an index measuring how dendritic the grains are. In addition, it is of interest to predict the macrosegregation pattern as a result of combined melt convection and grain movement.

In the following, the multiphase model is briefly outlined for completeness. This is then followed by a description of the numerical procedures. Representative numerical results are finally presented to shed light on the complicated solidification and multiphase flow phenomena occurring during equiaxed alloy solidification.

II. MATHEMATICAL FORMULATION

The physical system considered deals with solidification of an Al-4 wt pct Cu alloy in a two-dimensional (2-D) rectangular cavity of width 0.05 m and of height 0.1 m, as shown in Figure 1. The melt has an initial temperature of 930 K (the superheat is about 10 K) and initial concentration of 4 wt pct copper. The walls are impermeable and adiabatic, except for the west wall which is subject to convective cooling for $t > 0$. The coolant temperature is fixed at 293 K, and the convective heat-transfer coefficient between the coolant and the mold wall is chosen as 250 W/m^{2}K in all simulations presented subsequently. This set of parameters is representative of practical casting conditions and falls into the range of equiaxed dendritic solidification, as given by Kurz and Fisher.[5]

The multiphase approach to the modeling of equiaxed dendritic solidification has been thoroughly discussed in part I, and the model equations together with the supplementary relations presented therein are again summarized in Tables I and II, respectively. All symbols are defined in the Nomenclature, with the averaging symbols dropped for convenience. An overbar denotes an interfacial quantity. The model distinguishes three phases: the solid (ε_s), the interdendritic liquid (ε_d), and the extradendritic liquid (ε_l); and two interfaces: the solid/interdendritic liquid interface (S_s) and the dendrite envelope (S_e) separating the inter- and extradendritic liquids. One of the important assumptions made in the present multiphase model is that there exists a certain flow partitioning between the inter- and extradendritic regions. Hence, the relative portions of the mass flow rates through each region can be quantified by introducing an isotropic flow partition coefficient κ_v. This coefficient

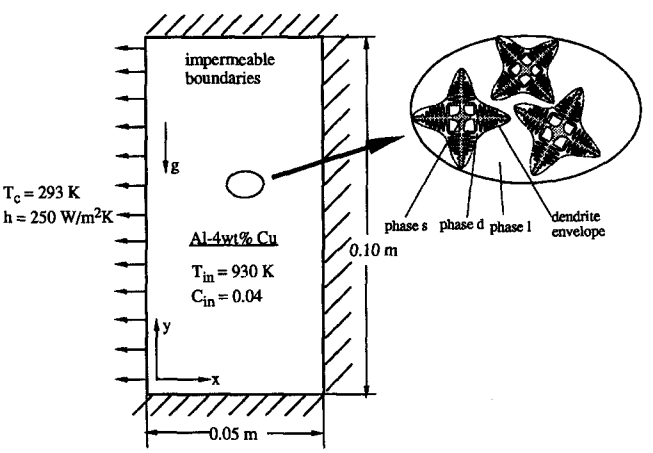

Fig. 1—Schematic of the physical system.

C.Y. WANG, Assistant Professor, is with the Department of Mechanical Engineering, University of Hawaii at Manoa, Honolulu, HI 96822. C. BECKERMANN, Associate Professor, is with the Department of Mechanical Engineering, The University of Iowa, Iowa City, IA 52242.

Manuscript submitted February 9, 1995.

Table I. Summary of a Multiphase Model

Continuity Equations

Solid phase (s)

$$\frac{\partial}{\partial t}(\rho_s \varepsilon_s) + \nabla \cdot (\rho_s \varepsilon_s \mathbf{v}_s) = \Gamma_s$$

Total liquid phase (f)

$$\frac{\partial}{\partial t}(\rho_f \varepsilon_f) + \nabla \cdot (\rho_f \varepsilon_f \mathbf{v}_f) = -\Gamma_s$$

Interfacial Species Balance (for Calculating Phase Change Rate)

$$(\overline{C}_e - \overline{C}_{sd})\Gamma_s = \frac{\rho_s S_s D_s}{l_{sd}}(\overline{C}_{sd} - C_s) + \frac{\rho_l S_e D_l}{l_{ld}}(\overline{C}_e - C_l) + [\rho_d \varepsilon_d \frac{\partial \overline{C}_e}{\partial t} + \rho_d \varepsilon_d \mathbf{v}_d \cdot \nabla \overline{C}_e - \nabla \cdot (\rho_d \varepsilon_d D_d^* \nabla \overline{C}_e)]$$

Momentum Equations

Solid phase (s)

$$\frac{\partial}{\partial t}(\rho_s \varepsilon_s \mathbf{v}_s) + \nabla \cdot (\rho_s \varepsilon_s \mathbf{v}_s \mathbf{v}_s) = -\varepsilon_s \nabla p + \nabla \cdot (\mu_s^* \varepsilon_s \nabla \mathbf{v}_s) + \mathbf{M}_s^d + \rho_s \varepsilon_s \mathbf{g}$$

Total liquid phase (f)

$$\frac{\partial}{\partial t}(\rho_f \varepsilon_f \mathbf{v}_f) + \nabla \cdot (\rho_f \varepsilon_f \mathbf{v}_f \mathbf{v}_f) = -\varepsilon_f \nabla p + \nabla \cdot (\mu_f^* \varepsilon_f \nabla \mathbf{v}_f) - \mathbf{M}_s^d + \varepsilon_f \rho_f \mathbf{g} + \nabla \cdot [\gamma \rho_f \varepsilon_f (\mathbf{v}_f - \mathbf{v}_s)(\mathbf{v}_f - \mathbf{v}_s)]$$

Species Equations

Solid phase (s)

$$\frac{\partial}{\partial t}(\rho_s \varepsilon_s C_s) + \nabla \cdot (\rho_s \varepsilon_s \mathbf{v}_s C_s) = \nabla \cdot (\rho_s \varepsilon_s D_s^* \nabla C_s) + \overline{C}_{sd}\Gamma_s + \frac{\rho_s S_s D_s}{l_{sd}}(\overline{C}_{sd} - C_s)$$

Total liquid phase (f)

$$\frac{\partial}{\partial t}(\rho_f \varepsilon_f C_f) + \nabla \cdot (\rho_f \varepsilon_f \mathbf{v}_f C_f) = \nabla \cdot (\rho_f \varepsilon_f D_f^* \nabla C_f) - [\overline{C}_{sd}\Gamma_s + \frac{\rho_s S_s D_s}{l_{sd}}(\overline{C}_{sd} - C_s)] + \nabla \cdot \{\rho_f \varepsilon_f (\mathbf{v}_f - \mathbf{v}_s)[C_f - \kappa_v C_d - (1-\kappa_v)C_l]\}$$

Mixture Energy Equation

$$\frac{\partial}{\partial t}[(\rho_s \varepsilon_s c_s + \rho_f \varepsilon_f c_f)T] + \nabla \cdot [(\rho_s \varepsilon_s c_s \mathbf{v}_s + \rho_f \varepsilon_f c_f \mathbf{v}_f)T] = \nabla \cdot [(\varepsilon_s k_s^* + \varepsilon_f k_f^*)\nabla T] + \Gamma_s[\Delta h + (c_s - c_l)T_E]$$

Auxiliary Relations for Secondary Variables

Interdendritic liquid fraction

$$\frac{\partial}{\partial t}(\rho_d \varepsilon_d) + \nabla \cdot (\rho_d \varepsilon_d \mathbf{v}_d) = S_e \rho_l \overline{w}_{ne} - \Gamma_s$$

Extradendritic liquid fraction

$$\varepsilon_l = \varepsilon_f - \varepsilon_d$$

Extradendritic liquid concentration

$$C_l = (\rho_f \varepsilon_f C_f - \rho_d \varepsilon_d \overline{C}_e)/(\rho_l \varepsilon_l)$$

Inter- and extradendritic liquid velocities

$$\mathbf{v}_d = \mathbf{v}_s + \kappa_v \frac{\rho_f \varepsilon_f}{\rho_d \varepsilon_d}(\mathbf{v}_f - \mathbf{v}_s);\ \mathbf{v}_l = \mathbf{v}_s + (1-\kappa_v)\frac{\rho_f \varepsilon_f}{\rho_l \varepsilon_l}(\mathbf{v}_f - \mathbf{v}_s)$$

was modeled in Wang *et al.*[6] and was found to depend only on volume fractions and characteristic length scales, as shown in Table II. As a result, only the momentum equation for the total liquid phase (f), consisting of the interdendritic liquid (d) and extradendritic liquid (l), needs to be solved, as shown in Table I. The individual liquid velocity fields, $\mathbf{v}_d$ and $\mathbf{v}_l$, can be algebraically obtained from the auxiliary relations also listed in Table I.

The velocity boundary conditions are the no-slip condition for the liquid velocity and zero normal component for the solid velocity. However, partial slip in the tangential direction may occur for the solid at the wall if the diameter of the solid particles is larger than the length scale of the surface roughness.[7] In the absence of experimental data, the model of Ding and Gidaspow[7] is adopted, where the tangential velocity of the solid is taken to be proportional to its normal gradient at the wall:

$$(\mathbf{v}_s)_t|_w = -\lambda_p \frac{\partial (\mathbf{v}_s)_t}{\partial n}\Big|_w \qquad [1]$$

where λ_p is the mean distance between particles and is given by

$$\lambda_p = \frac{d_e}{\varepsilon_g^{1/3}} \qquad [2]$$

with d_e and ε_g being the grain diameter and grain fraction, respectively. Note that for small d_e, the slip coefficient λ_p

Table II. Summary of the Supplementary Relations

Interfacial area concentrations:[4] $S_s = 2/\lambda_2$; $S_e = (36\pi)^{1/3} n^{1/3} (1 - \varepsilon_l)^{2/3}$

where $\lambda_2 = 50 \dot{T}^{-1/3}$ (μm)[23]

Grain density:[3] $\dfrac{\partial n}{\partial t} + \nabla \cdot (\mathbf{v}_s n) = \dot{n}$

Grain nucleation model:[8] $\dot{n} = n_0 \delta(T - T_N)$; $T_N = T_L(C_0)$

Grain growth model:[4,9] $\overline{w}_{ne} = \dfrac{4\sigma^* D_l m(\kappa - 1)\overline{C}_e}{\Gamma} a^2 \left(\dfrac{\Omega}{1-\Omega}\right)^{2b}$

where $a = 0.4567 + 0.173\ \mathrm{Pe}_\infty^{0.55}$; $b = 1.195 - 0.145\ \mathrm{Pe}_\infty^{0.16}$

Solid/liquid interfacial drag:[6] $\mathbf{M}_s^d = \varepsilon_f \beta^2 \dfrac{\mu_f}{R_e^2} \varepsilon_f (\mathbf{v}_f - \mathbf{v}_s)$

where $\beta = \dfrac{\beta_d}{[(1 - \varepsilon_l)^n + (\beta_d/\beta_l)^{2n}]^{1/2n}}$; $\beta_d = \dfrac{3\sqrt{5}}{(1 - \varepsilon_{si})^{3/2}} \dfrac{S_s}{\phi_e S_e}$;

$$\beta_l = \left\{ \frac{9}{2}(1 - \varepsilon_l) \frac{2 + 4/3(1 - \varepsilon_l)^5}{2 - 3(1 - \varepsilon_l) + 3(1 - \varepsilon_l)^5 - 2(1 - \varepsilon_l)^6} \frac{2\beta_d^2 (1 - \tanh \beta_d/\beta_d)}{2\beta_d^2 + 3(1 - \tanh \beta_d/\beta_d)} \right\}^{1/2};$$

$n = 0.176 \log \beta_d + 0.275$

Flow partition coefficient:[6] $\kappa_v = (1 - \varepsilon_l)(\beta/\beta_d)^2$

Interfacial species diffusion lengths:[10] $l_{sd} = d_s/6$; $\dfrac{d_e}{l_{ld}} = 2 + 0.865 \left(\dfrac{C_\varepsilon}{\varepsilon_l}\right)^{1/3} \mathrm{Pe}_e^{1/3}$

where $\mathrm{Pe}_\varepsilon = \dfrac{\varepsilon_l |\mathbf{v}_l - \mathbf{v}_s| d_e}{D_l}$; $C_\varepsilon = \dfrac{2 + \frac{4}{3}(1 - \varepsilon_l)^{5/3}}{2 - 3(1 - \varepsilon_l)^{1/3} + 3(1 - \varepsilon_l)^{5/3} - 2(1 - \varepsilon_l)^2}$

Macroscopic transport properties: $\mu_l^* = \mu_l$; $\mu_s^* = \dfrac{\mu_l}{\varepsilon_g} \left[(1 - \varepsilon_g/\varepsilon_g^c)^{-2.5\varepsilon_g^c} - (1 - \varepsilon_g) \right]$

$k_f^* = k_l$; $k_s^* = k_s$

$D_f^* = D_f$; $D_s^* = D_s$

Interfacial equilibrium relations: $\overline{C}_e = \dfrac{T - T_m}{m_l}$

$$\overline{C}_{sd} = \begin{cases} \kappa \overline{C}_e & \text{for primary solidification} \\ C_s & \text{for remelting} \\ \overline{C}_e & \text{for eutectic reaction} \end{cases}$$

approaches zero so that a no-slip condition for the grains results. Obviously, the preceding boundary condition requires experimental verification for solidification systems.

The interfacial transfer terms contained in the governing equations listed in Table I play a central role in the present multiphase model, since they physically reflect the intimate couplings between microscopic solidification phenomena and macroscopic transport phenomena. Determination of these interfacial terms requires the supplementary relations summarized in Table II. For completeness, brief explanations of these relations follow.

The interfacial area concentrations were obtained by assuming a platelike morphology for the dendritic solid/liquid interface and a spherical geometry for the dendrite envelope. The grain density needed for evaluation of the dendrite envelope area concentration is calculated from a conservation equation for the nuclei density (Table II), in which the term $\dot{n}$ represents the net generation rate accounting for both the birth and death of grains due to heterogeneous nucleation, remelting, dendrite arm pinch-off, agglomeration, and other effects. In the present work, the simplest nucleation model, namely, the instantaneous nucleation law proposed by Stefanescu *et al.*,[8] is employed. In this model, it is assumed that a certain number of nuclei instantaneously appear as soon as the temperature of the liquid melt falls below the nucleation temperature, T_N; *i.e.*, $\dot{n} = n_0 \delta(T - T_N)$, where n_0 is a constant and δ is the Dirac delta function. Moreover, it is assumed that nucleation can only occur if the local grain density before nucleation is equal to zero. This implies that no new grains will nucleate in the immediate neighborhood of existing grains. In the presence of solid movement, grains may be advected into regions of higher temperature and remelt to a sufficiently small diameter d_{si} (Table III). In this case, death of the grains takes place, and the present model instantaneously resets the local grain density to zero. The control volume in question is then allowed to renucleate later when the conditions are right. Grains may exist in regions of superheated melt as long as their diameter is above d_{si}. Considerable future research is needed to develop a model that more realistically captures the effects of convection on grain generation.

The dendrite envelope motion is governed by the growth of dendrite tips. For convection-dominated growth,

Table III. Thermophysical Properties and Empirical Constants for Al-4 Wt Pct Cu Alloy

Property Data	
Density of the liquid phase, ρ_f (kg/m^3) (except in buoyancy term)	2450
Density of the solid phase, ρ_s (kg/m^3) (except in buoyancy term)	2450
Density of the solid phase in buoyancy term, (kg/m^3)	2558
Dynamic viscosity of the liquid phase μ_f (N s/m^2)	0.0012
Thermal conductivity of the liquid phase, k_f (W/m K)	77
Thermal conductivity of the solid phase, k_s (W/m K)	153
Specific heat of the liquid phase, c_f (J/kg K)	1179
Specific heat of the solid phase, c_s (J/kg K)	766
Latent heat of fusion at T_E, Δh (J/kg)	3.97×10^5
Mass diffusivity of the liquid phase, D_l (m^2/s)	5.0×10^{-9}
Mass diffusivity of the solid phase, D_s (m^2/s)	8.0×10^{-13}
Segregation coefficient, κ (wt pct/wt pct)	0.173
Liquidus temperature of the initial melt, T_L (C_{in}) (K)	919.7
Eutectic temperature, T_E (K)	821.2
Eutectic concentration, C_E (wt pct of Cu)	32.7
Melting temperature of Al, T_m (K)	933.5
Gibbs–Thomson coefficient, Γ (m K)	2.41×10^{-7}
Empirical Constants	
Maximum grain packing fraction, ε_g^c	0.637
Initial grain diameter, d_{si} (m)	10^{-6}

a correlation obtained by curve-fitting the Stokes' solution due to Ananth and Gill[9] is adopted. The solid/liquid interfacial drag in equiaxed systems has been modeled by Wang *et al.*,[6] who derived an expression valid for all solid fractions.

Local thermal equilibrium is assumed due to the large value of the Lewis number for metal alloys. Of course, solutal undercooling, which is critical in equiaxed alloy solidification, is taken into account. The expressions used for the interfacial species diffusion lengths in the solid and ahead of the dendrite envelope are also given in Table II. The macroscopic or effective thermal conductivities, mass diffusivities, and liquid viscosity are assumed equal to their microscopic counterparts. The expression for the effective solid viscosity shown in Table II was derived based on available models for flow of solid/liquid mixtures.[10] It should be stressed here that for dendritic structures, the solid viscosity is not directly dependent on the solid fraction but rather on the grain fraction. As soon as the grain fraction reaches the packing limit, the grains will impinge upon each other and form a coherent and rigid microstructure. Again, many of the expressions in Table II should only be viewed as reasonable estimates, and future research should concentrate on improving their accuracy for solidification systems.

Finally, interfacial thermodynamic equilibrium with a linear phase diagram is assumed. The densities of the solid and liquid phases are taken to be equal and constant, except for the ones in the buoyancy terms. Hence, volume contraction or expansion during solidification is neglected. For the buoyancy term in the liquid momentum equation, the liquid density is allowed to vary with the liquid temperature and species concentration, so that thermosolutal convection is fully considered. The relation between density, temperature, and concentration for the liquid phase is taken from Ganesan and Poirier,[11] *i.e.*,

$$\rho_f = \frac{1000}{0.397 - 4.522\times10^{-3}C_f + 4.0924\times10^{-5}T + 1.1078\times10^{-6}C_fT + 2.7475\times10^{-5}C_f^2} \quad [3]$$

where the temperature T is in degree Celcius and the concentration C_f in weight percent. From Eq. [3], the ratio of solutal to thermal buoyancy can be estimated to be approximately 30. The positive value indicates that the solutal and thermal buoyancy forces in and near the mushy zone augment each other. The fact that the ratio is much larger than unity implies that the solutal buoyancy forces are dominant.

The solid density is approximately constant at a value of 2558 kg/m^3,[11] which is larger than the liquid density at the initial composition. Hence, crystal sedimentation is expected during the early stages of solidification. Later into solidification, it is possible that the liquid concentration exceeds 10 wt pct Cu, a threshold point at which the liquid-phase density becomes larger than the solid-phase density;[11] however, crystal movement is most likely terminated at these stages because of the significant solidification that occurred earlier. Other thermophysical properties and empirical constants used in the simulations are compiled in Table III.

III. NUMERICAL PROCEDURES

In this study, a fully implicit control-volume-based finite difference method, in conjunction with a multiple time-step scheme, is employed to discretize the strongly coupled and highly nonlinear model equations presented in Table I. Numerical details for treating the phase change and predicting both macro- and microscopic behaviors are elaborated in Sections A through C.

A. *Control-Volume-Based Finite Difference Method for Multiphase Systems*

The model equations presented in Table I for multiphase systems with solidification take the following general form:

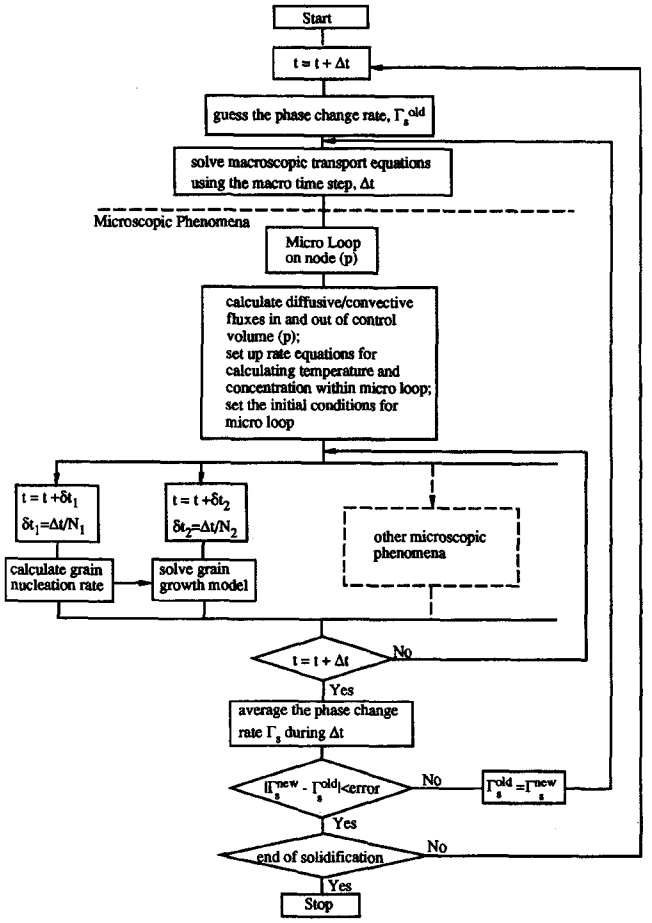

Fig. 2—Flow chart of multiple time-step scheme for coupled macroscopic transport phenomena and microscopic solidification phenomena.

$$\frac{\partial(\varepsilon_k \rho_k \Psi_k)}{\partial t} + \nabla \cdot (\varepsilon_k \rho_k \mathbf{v}_k \Psi_k) = \nabla \cdot (\varepsilon_k \Gamma_k^* \nabla \Psi_k) + S_k \quad [4]$$

where Γ_k^* stands for the diffusion coefficient of a general transfer field Ψ_k and S_k represents all the source terms for the transport of Ψ_k, including the interfacial interaction terms among the phases. Notice that all the governing equations shown in Table I are equally applicable to the fully solid, mushy, and fully liquid regions. Therefore, they can be solved using a fixed-grid, single-domain numerical solution procedure. Equation [4] can be discretized using a control-volume-based finite difference method,[12] in which the transient term is treated fully implicitly. Details of the derivation of the discretization equation are provided elsewhere[12] and thus are not repeated. Here, suffice it to mention that the upwind scheme is used for the advection terms. For discretizing the momentum equations, a staggered grid is employed.

The flow fields of the various phases in a multiphase system interact with each other in numerous ways, *e.g.*, through the constraint that the phases have to share the same volume at a time (*e.g.*, $\Sigma\varepsilon_k = 1$) and through a common pressure term. These difficulties have been adequately resolved by the so-called IPSA algorithm developed by Spalding,[13] *i.e.*, the interphase slip algorithm. This IPSA algorithm, as a basic feature of the commercial CFD code PHOENICS, is employed in the numerical implementation of the present multiphase model for solidification problems.

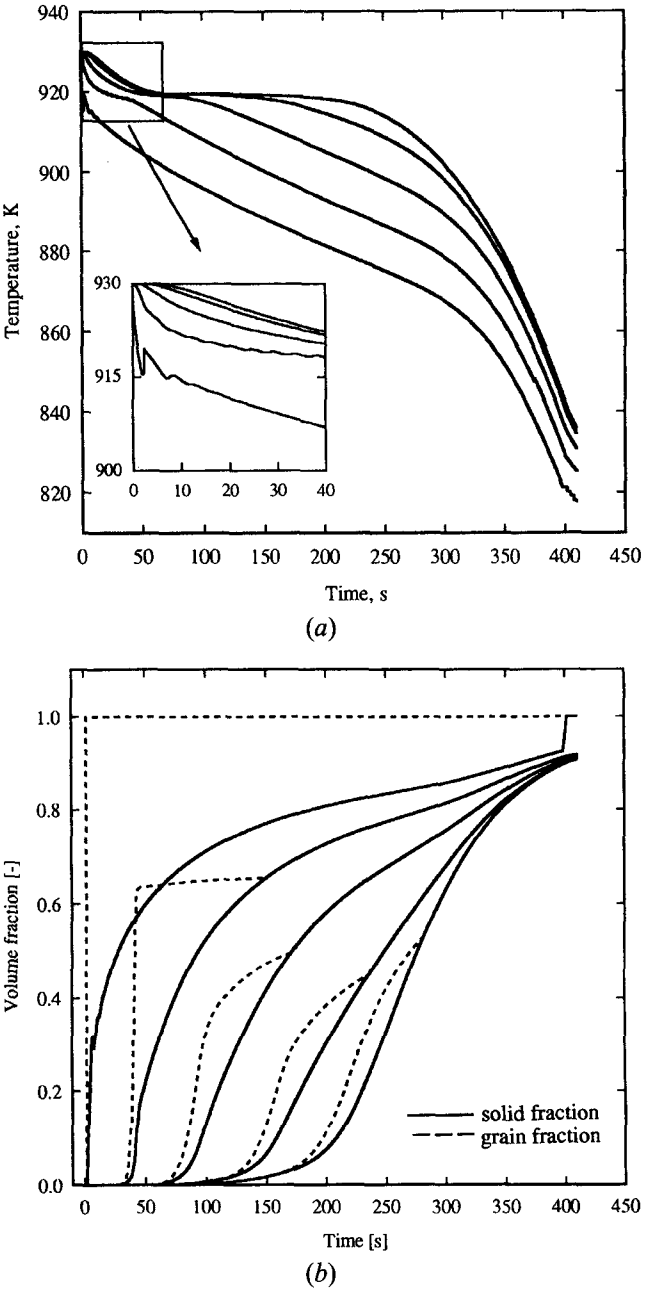

Fig. 3—(*a*) Cooling curves and (*b*) solid and grain fraction evolutions in diffusion-controlled equiaxed dendritic solidification (case I). The curves from left to right correspond to five interior locations of the casting, with the (*x*, *y*) coordinates being (0.0625, 1.25), (11.825, 23.75), (24.375, 48.75), (36.875, 73.75), and (49.375, 98.75) in units of millimeter.

A detailed discussion of the solution algorithm along with its single-phase version, SIMPLER, can be found in the preceding references and is not repeated here.

The discretization equations are solved iteratively in the following sequence.

(1) Guess the phase change rate Γ_s by taking the value from the previous time-step (zero for the first time-step).
(2) Compute the flow fields $\mathbf{v}_s$ and $\mathbf{v}_f$ from the continuity and momentum equations by the IPSA algorithm.
(3) Compute the volume averaged concentration fields C_s and C_f from the species conservation equations.

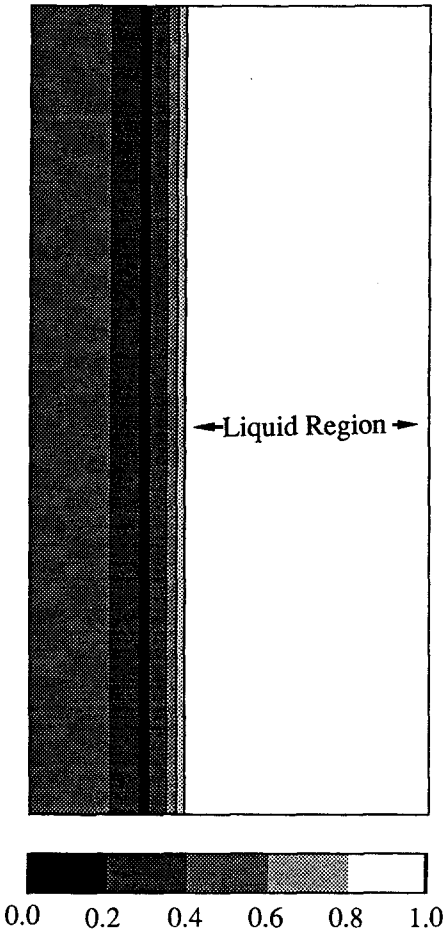

Fig. 4—Internal solid fraction distribution at t = 50 s for case I.

(4) Compute the temperature field T from the mixture energy equation.
(5) Calculate the liquidus temperature from C_f:
$T_L(C) = T_m + m_l C_f$
and check if the cell is within the mushy zone:
if $T > T_L(C)$ or $T < T_E$ (*i.e.*, not in the mushy zone), set $\Gamma_s = 0$ and go back to step (2).
if $T_E \le T < T_L(C)$ (*i.e.*, in the mushy zone), go on to the next step.
(6) Determine the nucleation rate according to the nucleation model shown in Table II, and calculate the grain density n from the conservation equation also shown in Table II.
(7) Calculate the phase change rate Γ_s from the interfacial species balance given in Table I. More details are provided in Section B. It should be cautioned that special and careful considerations are required for calculating the phase change rate in order to develop a numerically robust algorithm for solidification problems.
(8) Feed the newly obtained Γ_s back to step (2).
(9) Repeat steps (1) through (8) until convergence of all fields is achieved, before advancing to the next time-step.

B. *Multiple Time-Step Scheme*

In the foregoing multiphase model for dendritic solidification, the phase change rate represents a critical parameter reflecting the intricate couplings between the microscopic submodels for grain nucleation and growth, and the macroscopic model for transport phenomena. The temperature, concentration, and flow fields predicted from the macroscopic model are used to calculate the nucleation rate, grain growth rate, and hence the phase change rate during solidification. The phase change rate so estimated, in turn, exerts a significant influence on momentum transfer through changing the phase volume fractions, energy transfer through releasing the latent heat, and species transport through rejecting or incorporating species at the solid/liquid interface. Furthermore, in the present problem, due to the presence of multiple length scales, time scales at which various physical phenomena evolve are significantly disparate. For example, the evolution of the grain fraction is dictated by dendrite tip growth, which is a much faster

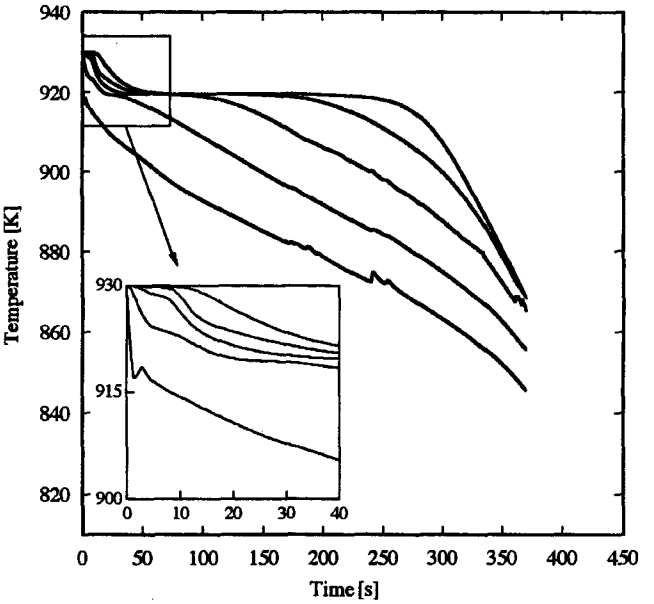

(*a*)

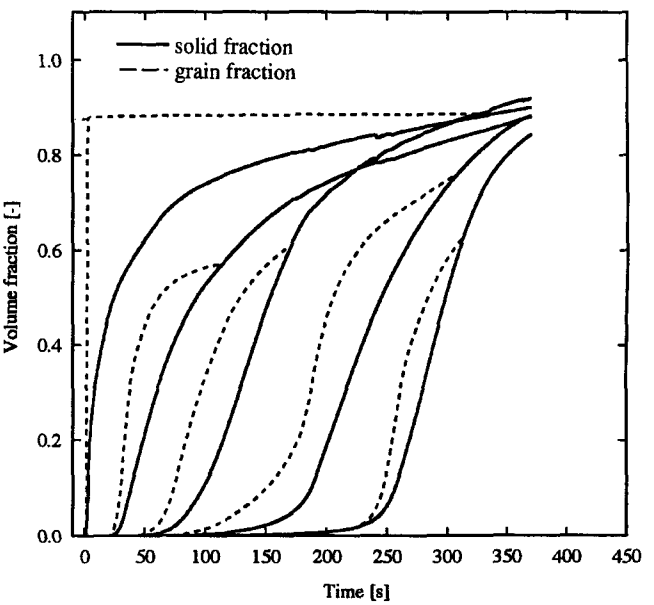

(*b*)

Fig. 5—(*a*) Cooling curves and (*b*) solid and grain fraction evolutions in equiaxed dendritic solidification with a stationary solid (case II) for the same five interior locations as in Fig. 3.

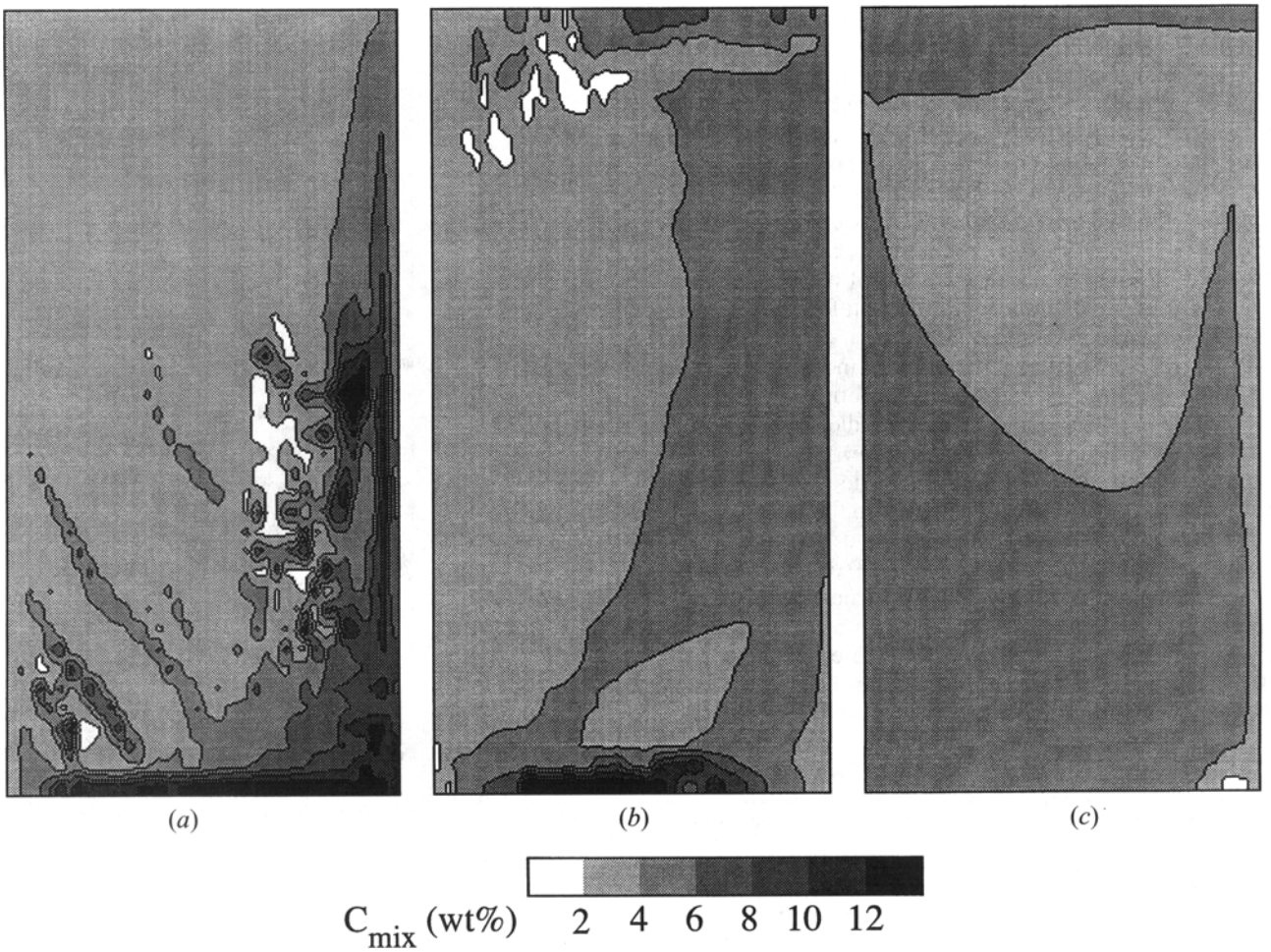

Fig. 6—Final macrosegregation patterns for cases II through IV: (*a*) case II (stationary solid, $n_0 = 10^9$ m^{-3}), (*b*) case III (moving solid, $n_0 = 10^9$ m^{-3}), and (*c*) case IV (moving solid, $n_0 = 10^{11}$ m^{-3}).

physical process than the macroscopic transport; accurate modeling of microstructure hence requires a very fine time-step.[14] However, a large time-step is desirable for the macroscopic conservation equations summarized in Table I, particularly in 2-D and three-dimensional (3-D) situations. To remedy the difficulty, a multiple time-step coupling scheme, inspired by Thévoz *et al.*,[2] is proposed. Figure 2 shows a flow chart illustrating the scheme as well as the interactions between the multiple time-step levels.

In the present article, where an instantaneous nucleation model is assumed, a two time-step scheme is adequate. That is, a macro time-step is used for solving the macroscopic transport fields and a micro time-step is used for accurately simulating the grain growth and hence microstructural development. The total phase change rate during a macro time-step, Δt, as calculated from this microloop, is then fed back to the momentum, energy, and species equations for correction of the flow, temperature, and concentration fields. The whole process is interactively repeated until convergence is achieved. Experience shows that $N = 10$ already gives satisfactory results. Detailed numerical implementation of the multiple time-step scheme has been explained elsewhere.[15]

The integration of the multiple time-step scheme into the control-volume method provides an efficient and stable procedure for numerically treating the micro- and macroscopic coupling in the presence of convection. The algorithm reduces to a form similar to the one proposed by Thévoz *et al.*[2] in the diffusion case. The slight differences lie in that the present one allows for a complete coupling between the heat and solute diffusion processes (we iteratively solve the energy equation and interfacial species balance), whereas the scheme by Thévoz *et al.* does not feed the calculated solid fraction variation back into the energy equation for rectifying the temperature field. Therefore, the present scheme alleviates most of the stability and convergence problems encountered in Thévoz *et al.*

C. *Other Numerical Considerations*

Other numerical details to ensure stable and fast convergence include certain considerations for the eutectic reaction and the remelting process. During the eutectic reaction, both the solid and liquid interfacial concentrations $\overline{C}_{sd}$ and $\overline{C}_e$ are equal to C_E, so that the interfacial species balance listed in Table I becomes trivial. Instead, the phase change rate can be calculated from the mixture energy equation using the large source technique proposed by Voller.[16]

The remelting process is numerically modeled by assuming that the solute content released to the liquid is equal to the average concentration in the solid phase, as shown in Table II. The approximation eliminates the need to record

the histories of the concentration profile in the solid phase. Also, note that this approximation becomes exact when the solid is solutally well mixed. The reader can consult Wang[10] for other details of the numerical implementation of the multiphase model and several validation studies.

For the simulations presented in Section IV, the computational domain is divided into a 40 × 40 grid. This mesh was selected based on a compromise between accuracy and computational time. Several preliminary calculations conducted for different meshes indicated that the 40 × 40 grid system is able to capture all solidification features at a reasonable computational cost, whereas coarser meshes were unable to reveal certain localized phenomena, such as the formation of channel segregates. A uniform grid was chosen because the locations of strong gradients in the macroscopic variables are not known *a priori.*

Different time-steps were used for various simulations to ensure that the sensitivity of the results to the time-step was minimized in each case. In the first two cases to be described in Section IV, a time-step of 0.05 seconds was used, although the time-step for the first diffusion case could be larger. In the last two cases, a time-step of 0.025 seconds was employed in the first half and doubled in the second half of the simulations. Iterations performed within each time-step were terminated when changes in the overall species and energy balances fell below 0.001 pct. The calculations were performed on HP* 715/50 and IBM** 3090 computers, and each 1-second of real-time simulation required approximately 30, 360, 720, and 720 CPU seconds on the IBM 3090 computer for the first, second, third, and fourth cases, respectively.

*HP is a trademark of Hewlett-Packard Company, Colorado Springs, CO.

**IBM is a trademark of International Business Machines Corp., Armonk, NY.

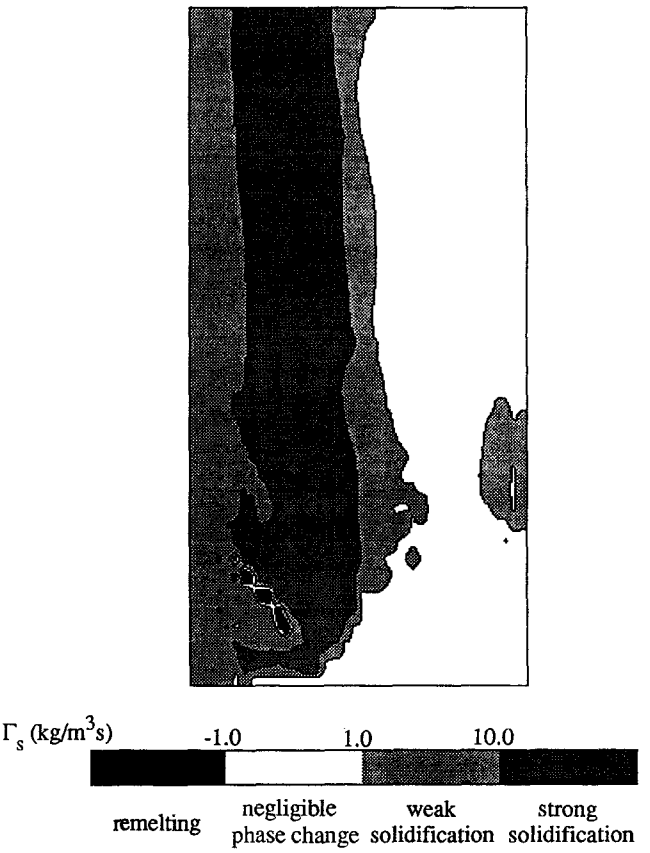

Fig. 7—Predicted phase change rate for case II at t = 90 s showing remelting inside a segregated channel.

IV. RESULTS AND DISCUSSION

A total of four different simulations were performed. With the same nucleation rate constant of $n_0 = 10^9$ m^{-3}, the first three cases examine the effects of melt convection and solid transport. In case I, both melt convection and solid movement are neglected so that solidification is controlled solely by diffusion. In contrast, the second case includes the influence of melt convection while assuming a stationary solid, while the third case considers both melt convection and solid transport. Otherwise identical to case III, the last case features a higher nucleation rate constant of $n_0 = 10^{11}$ m^{-3}. This case can be viewed to correspond to a grain-refined casting.

A. *Case I: Diffusion-Controlled Solidification*

This is a base case for all the following simulations including convection. In addition, this case is representative of a microgravity environment, where both liquid flow and solid movement diminish.

In the absence of flow, solidification occurs in a one-dimensional manner. The cooling curves and the solid and grain fraction evolutions at five different locations inside the casting are shown in Figures 3(a) and (b), respectively. The x and y coordinates of the five locations are given in the figure captions. It can be seen from the inset of Figure 3(a) that the first cooling curve in the immediate neighborhood of the mold wall undergoes a marked recalescence period which is characteristic of equiaxed solidification. The other cooling curves corresponding to the interior of the casting, however, exhibit thermal plateaus because of decreased cooling rates. Between t = 395 and 402 seconds the eutectic reaction occurs in the first computational cell. The simulation is terminated at t = 402 seconds, since no interesting phenomena follow.

As can be seen from Figure 3(b), the grain growth is rapid in the cell nearest to the cold wall, where the cooling rate is the highest, but becomes slower inside the domain because of the lower cooling rates. Except for the first location, the grain fraction curves (dashed lines) merge to the solid fraction curves (solid lines) at certain intermediate times, implying that the grain growth thereafter occurs in a globulitic manner. This is because the extradendritic liquid is continuously enriched by the solute rejected during solidification, and consequently, the undercooling, which drives the grain growth, diminishes.

For brevity, no distributions of temperature and solid fraction are presented here, except that Figure 4 illustrates the internal solid fraction distribution at t = 50 seconds. The internal solid fraction is defined as the ratio of the solid fraction to the grain fraction and is thus a direct measure of the dendritic structure of the crystals. The lower the internal solid fraction, the more dendritic the equiaxed crystals are. An internal solid fraction of unity corresponds to a globulitic crystal. Since the tiny nuclei appear in a globulitic form, the internal solid fraction was initialized to

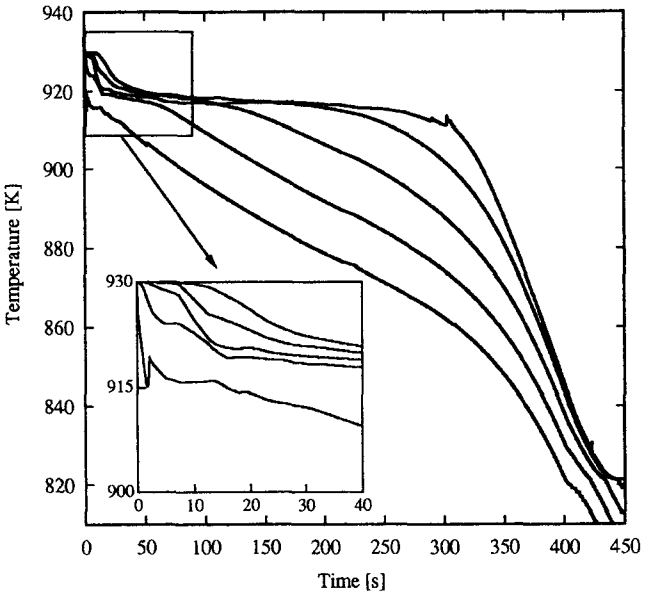

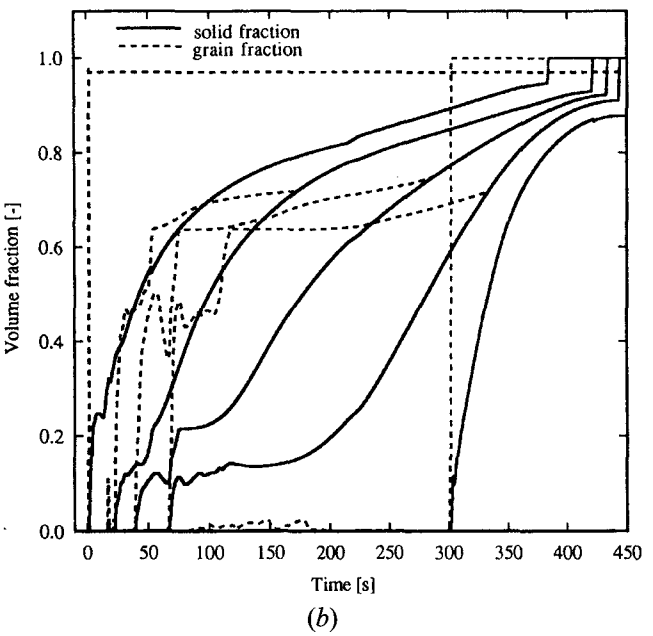

Fig. 8—(*a*) Cooling curves and (*b*) solid and grain fraction evolutions in equiaxed dendritic solidification with melt convection and solid movement (case III) for the same interior locations as in Fig. 3.

unity. Thus, the pure liquid as well as the edge of the mushy zone appears as a white region in Figure 4. Just behind the liquidus isotherm, the dendrite tip undercooling is largest and the nuclei quickly develop into highly dendritic crystals with an internal solid fraction below 0.2. After impingement of the grains and further within the mushy zone, thickening of the dendrite arms due to significant solidification causes a continual increase in the internal solid fraction toward the cooled wall.

B. *Case II: Solidification with Melt Convection*

In this case, the solid is still not allowed to move, implying that the equiaxed grains are fixed in space as soon as they nucleate. However, thermosolutal convection in the liquid melt is fully considered. For the alloy under consideration, the heavier copper is rejected during solidification, so that both solutal and thermal buoyancy forces cause a downward flow near the cold wall.

Figures 5(a) and (b) illustrate the cooling curves and solid and grain fraction evolutions at the same locations as in case I. Again, a recalescence is clearly seen in the first cooling curve of Figure 5(a) for the same reason as explained earlier. Overall, the cooling curves are qualitatively similar to the ones in diffusion-dominated solidification, although the temperatures are different in magnitude. For the nodes located in the lower portion of the cavity, slight temperature oscillations seem to occur at about $t = 250$ seconds (Figure 5(a)), which is probably due to resolidification of solute-rich liquid within channels that developed in the lower left part of the cavity (subsequent discussion). From Figure 5(b), it can be seen that the equiaxed grains in the first cell undergo free growth, while the grain growth at the four internal locations slows down due to the increase in the concentration of the extradendritic liquid as solute-rich fluid is advected into these regions. Consequently, the grain fractions during solidification are lower in the interior of the casting.

The detailed time evolutions of the solidification and transport behaviors are documented in Wang[10] and are not presented here for brevity. Only the final compositional and structural features of case II are briefly discussed subsequently. The shaded final macrosegregation plots shown in Figure 6 are of the mixture concentration, *i.e.*,

$$C_{\text{mix}} = \varepsilon_s C_s + \varepsilon_f C_f \qquad [5]$$

with a single scale applied to all figures. The physical cause of macrosegregation is the movement of liquid relative to the solid phase during solidification.

Overall, the final macrosegregation shown in Figure 6(a) for case II indicates positive segregation at the bottom of the cavity. This is at the expense of negatively segregated regions at the top and in the middle so that the global species balance is maintained. Several channel segregates can be observed. The solute-enriched fluid feeding a channel depresses the local liquidus temperature, thereby reducing the solidification rate and/or causing partial remelting. The channel, in turn, provides a preferred path for the downward flow of the solute-rich liquid. The presence of more solute-rich liquid in the channel reduces solidification further. The outcome of this runaway phenomenon is the formation of a channel segregate.

The present type of channel segregates has been previously observed in laboratory experiments using Al-Cu alloys.[17] A similar type, oriented in the opposite direction, located at the top of a casting and called "A" segregates, has been widely predicted for other alloy systems.[18,19,20] It is well established by experiments (*e.g.*, Reference 21) that the direction of channel segregates depends on the sign of the density change and hence the flow direction. In an alloy such as Al-4 wt pct Cu, the liquid flow is downward, and hence the positively segregated channels turn downward, as predicted in the present study. In other systems, such as NH_4Cl-H_2O and Pb-Sn alloys, where the flow is upward, the usual A segregates appear. Both types of segregates can be attributed to the same physical mechanisms. It must be cautioned that channels are 3-D in nature. Therefore, 2-D simulations may not be realistic.

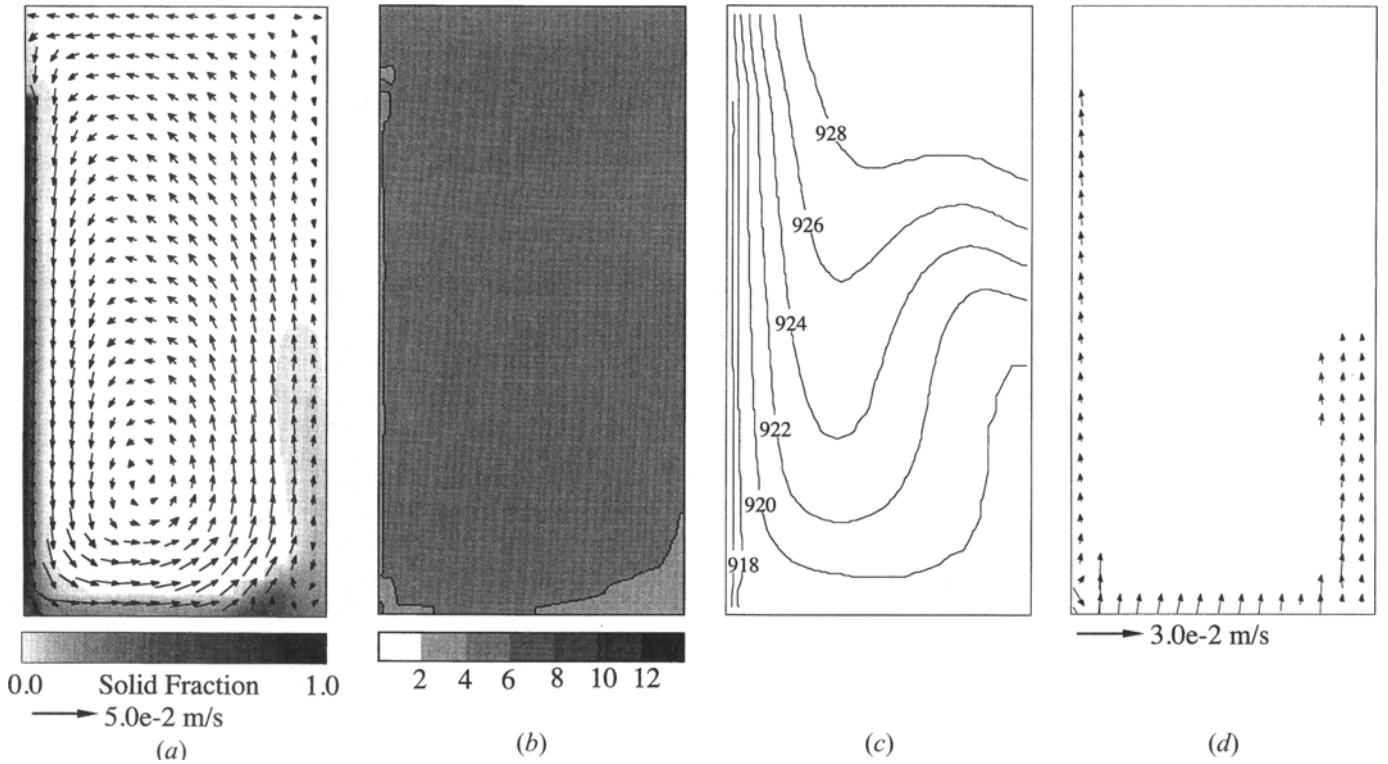

Fig. 9—Results for case III at t = 10 s: (*a*) solid fraction and liquid velocity vectors, (*b*) mixture concentration (wt pct), (*c*) isotherms (in K), and (*d*) relative velocity vectors ($\mathbf{v}_f - \mathbf{v}_s$).

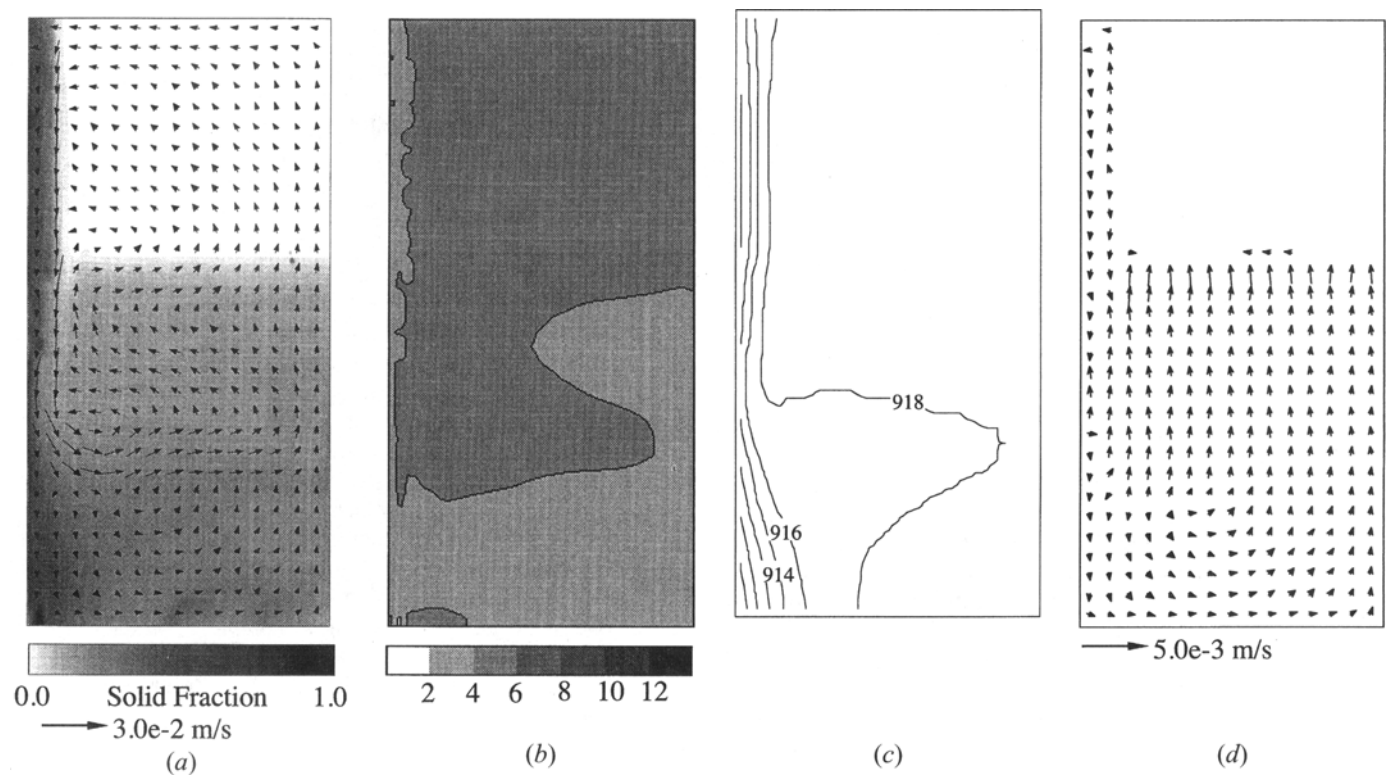

Fig. 10—Results for case III at t = 50 s: (*a*) solid fraction and liquid velocity vectors, (*b*) mixture concentration (wt pct), (*c*) isotherms (in K), and (*d*) relative velocity vectors ($\mathbf{v}_f - \mathbf{v}_s$).

To understand the formation of channel segregates, much research has been conducted in the past 3 decades.[22] Most previous work speculates that localized remelting is a major mechanism for channel formation. However, conclusive experimental evidence for metal alloys is still lacking due to the extreme difficulty in forecasting the channel locations, arranging proper measurements before the channels start to develop, and finally determining the phase change rate in-

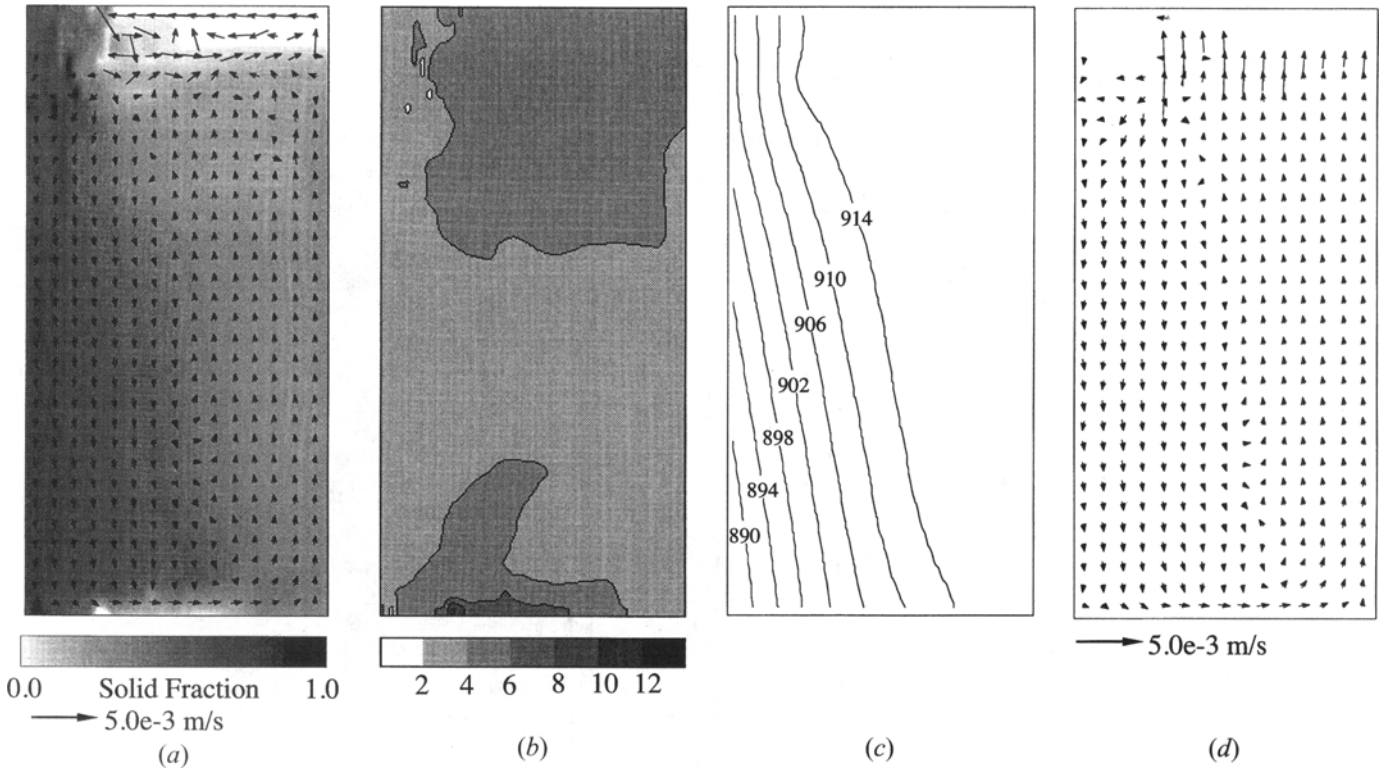

Fig. 11—Results for case III at t = 150 s: (*a*) solid fraction and liquid velocity vectors, (*b*) mixture concentration (wt pct), (*c*) isotherms (in K), and (*d*) relative velocity vectors ($\mathbf{v}_f - \mathbf{v}_s$).

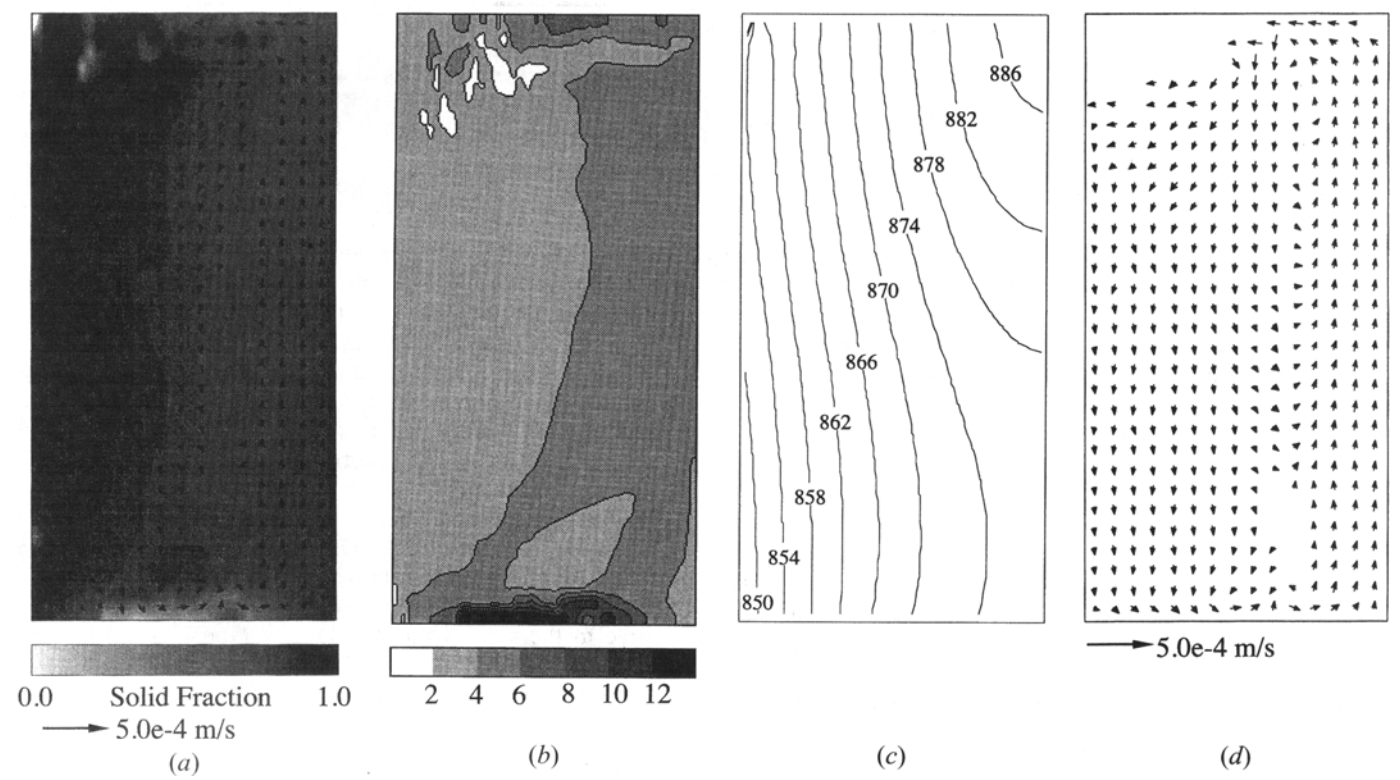

Fig. 12—Results for case III at t = 350 s: (*a*) solid fraction and liquid velocity vectors, (*b*) mixture concentration (wt pct), (*c*) isotherms (in K), and (*d*) relative velocity vectors ($\mathbf{v}_f - \mathbf{v}_s$).

side these tiny channels. In order to study the channel formation in more detail, Figure 7 shows the phase change rate at t = 90 seconds. It can be seen that remelting occurs nowhere but inside the second channel from the bottom (corresponding to Figure 6(a)). This evidence indicates, at least theoretically, that the formation of channel segregates

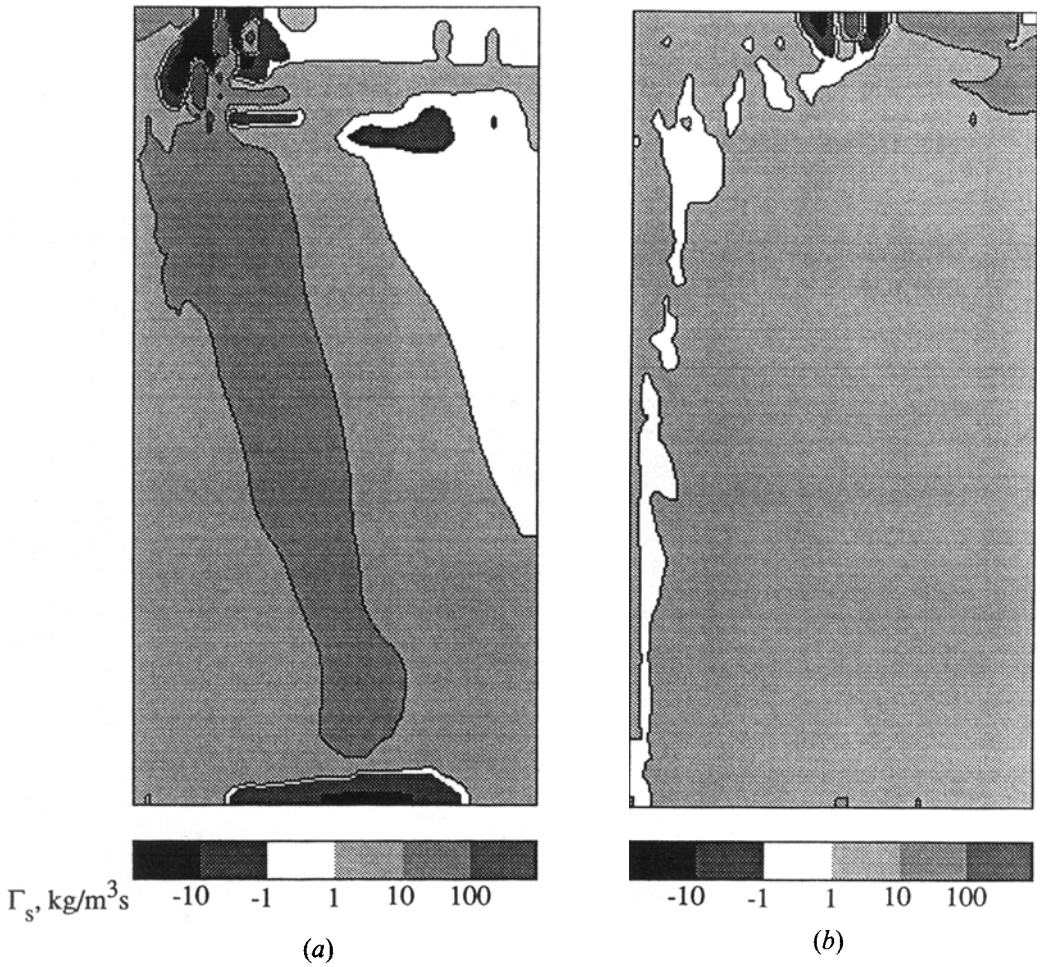

Fig. 13—Predicted phase change rate for case III at (*a*) t = 140 s and (*b*) t = 350 s.

is accompanied by localized remelting. Nonetheless, remelting may not be a necessary condition for the initiation of channel segregates. It would be of interest to see whether remelting also occurs in the channel segregates predicted elsewhere.[18,19,20]

In the absence of solid transport, the final grain size distribution in case II is determined solely by nucleation and hence remains uniform at a radius of 0.62 mm, corresponding to $n_0 = 10^9$ (m^{-3}).

C. *Case III: Solidification with Melt Convection and Solid Movement*

This case features both liquid and solid motion, thus requiring the full multiphase model proposed in Section B. The predicted cooling curves and the solid and grain fraction evolutions are shown in Figures 8(a) and (b), respectively. They should be compared to Figures 3(a) and (b) for the diffusion case and Figures 5(a) and (b) for the case with a stationary solid. While the cooling curves strongly resemble those for cases I and II, the solid and grain fraction evolutions have a distinctive feature: oscillating solid and grain fractions occur at certain times at the internal locations. Furthermore, it can be noticed that both fractions oscillate in phase. The oscillations have a period of the order of several seconds, while the numerical time-step was 0.025 seconds, indicating that they are accurately resolved. They can be explained by the highly transient nature of the grain movement at particular locations, and no oscillations appear after the grain fraction reaches the packing limit.

Figures 9 through 12 show the solidification and transport behaviors at times t = 10, 50, 150, and 350 seconds, respectively. These figures include the solid fraction, liquid velocity, mixture concentration, temperature, and relative velocity distributions. The liquid velocity vector plots are superimposed on the solid fraction images, with a velocity scale shown below each plot. For clarity, the velocity vectors are interpolated to a coarser grid than used in the computations. The solid fraction images are produced using a continuous spectrum of gray scales. The isotherms are in equal increments. The relative velocity vectors, $\mathbf{v}_f - \mathbf{v}_s$, are also displayed to illustrate the movement of the liquid relative to the solid. Note that for a stationary solid (*i.e.*, $\mathbf{v}_s = 0$), the relative velocity simply represents the liquid velocity through the packed crystal bed.

1. *Early stages of solidification*

At an early stage of solidification (*i.e.*, t = 10 seconds), the liquid flow field (Figure 9(a)) consists of a single counterclockwise rotating convection cell. The liquid flow in this case is not only driven by thermosolutal convection but also by the sedimentation of the forming solid. The downward flow of the solid adjacent to the cold wall, due to its higher density than the liquid, exerts a large interfacial drag

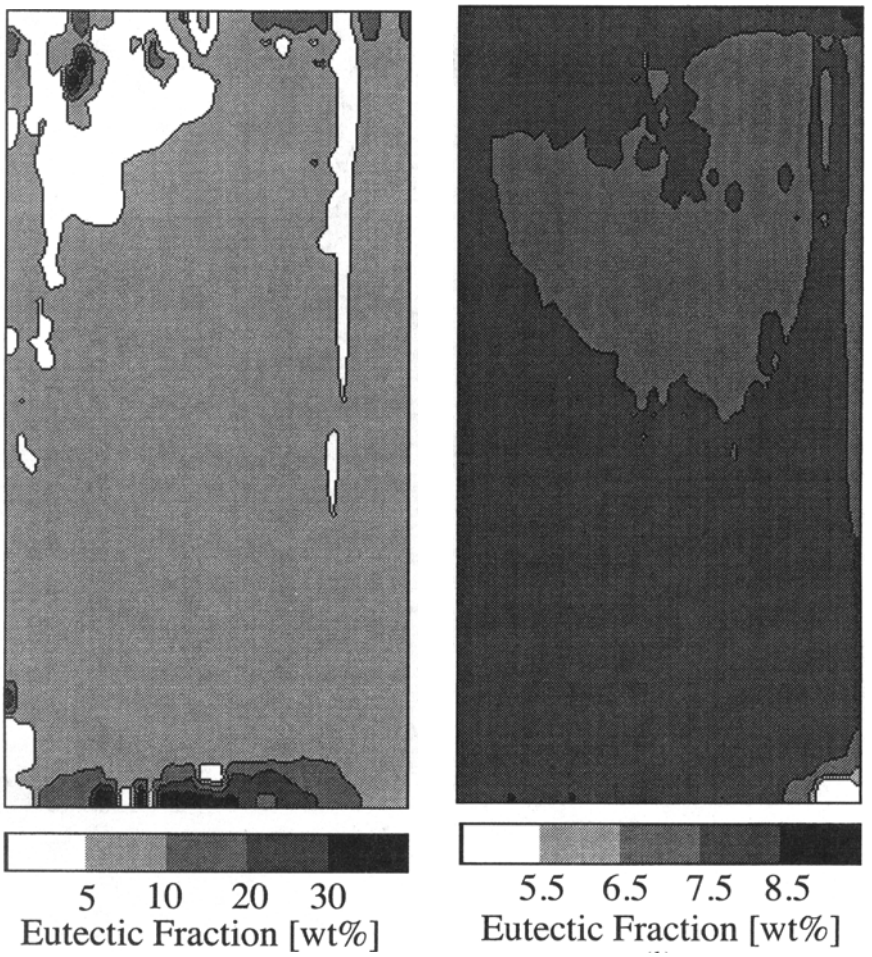

Fig. 14—Eutectic fraction distributions in (*a*) case III and (*b*) case IV.

on the liquid and pulls the liquid downward. This sedimentation-driven liquid flow further augments the thermal and solutal buoyancy forces in the liquid. Convection driven by sedimentation has been researched little and deserves more attention.

The solid fraction distribution shown in Figure 9(a) indicates that some solid crystals, that nucleated and grew along the left cold wall, are swept by the liquid flow into the superheated region near the right wall. The mixture concentration plot shown in Figure 9(b) also illustrates this trend, since negative segregation associated with the initially forming solid appears in the lower right corner. The isotherms shown in Figure 9(c) greatly deviate from the vertical due to convection effects.

The relative velocities shown in Figure 9(d) are mostly upward, demonstrating that the downward component of the solid velocity is larger than the one of the liquid. This is a direct evidence of crystal sedimentation. In the bulk liquid region, the small nuclei cause such a large interfacial drag that the relative velocity vanishes.

Results at $t = 50$ seconds (Figure 10(a)) show an extensive mushy zone forming in the lower portion of the cavity. A crystal sediment bed appears, implying that sedimentation is a dominant phenomenon in equiaxed solidification, especially for the low grain density (*i.e.*, $n_0 = 10^9$ m^{-3}) and hence large crystal sizes in the present case. In the bottom fourth of the cavity, a coherent and dense network of dendrites forms, which offers a large resistance to the liquid flow, forcing the liquid to bypass it. Above this bottom packed bed, the multiphase flow in the mushy zone and the pure liquid flow near the top strongly interact with each other.

The region of negative segregation further penetrates into the domain in the direction of the solid motion, as can be seen from Figure 10(b). The negative segregation is strongest at the bottom where the solute-poor crystals have settled. The isotherm plot in Figure 10(c) shows an interesting feature: the lower-right corner below the 918 K isotherm is as warm as the upper portion of the cavity. This is a direct consequence of the downward motion of the solid, which shifts the locations where solidification occurs. Because of the high solidification rate of the sedimenting crystals (*e.g.*, the slope of the solid fraction curves in Figure 8(b) at 50 seconds), a significant amount of latent heat is released in the lower portion keeping the local temperature high.

The relative velocities shown in Figure 10(d) are still mostly upward, particularly in the regions above the bottom packed bed. Inside the packed bed, where the grain fraction is greater than the packing limit, the crystals do not move, and thus the relative velocity vectors reflect the liquid velocity only. A weak liquid recirculation is seen inside this packed bed.

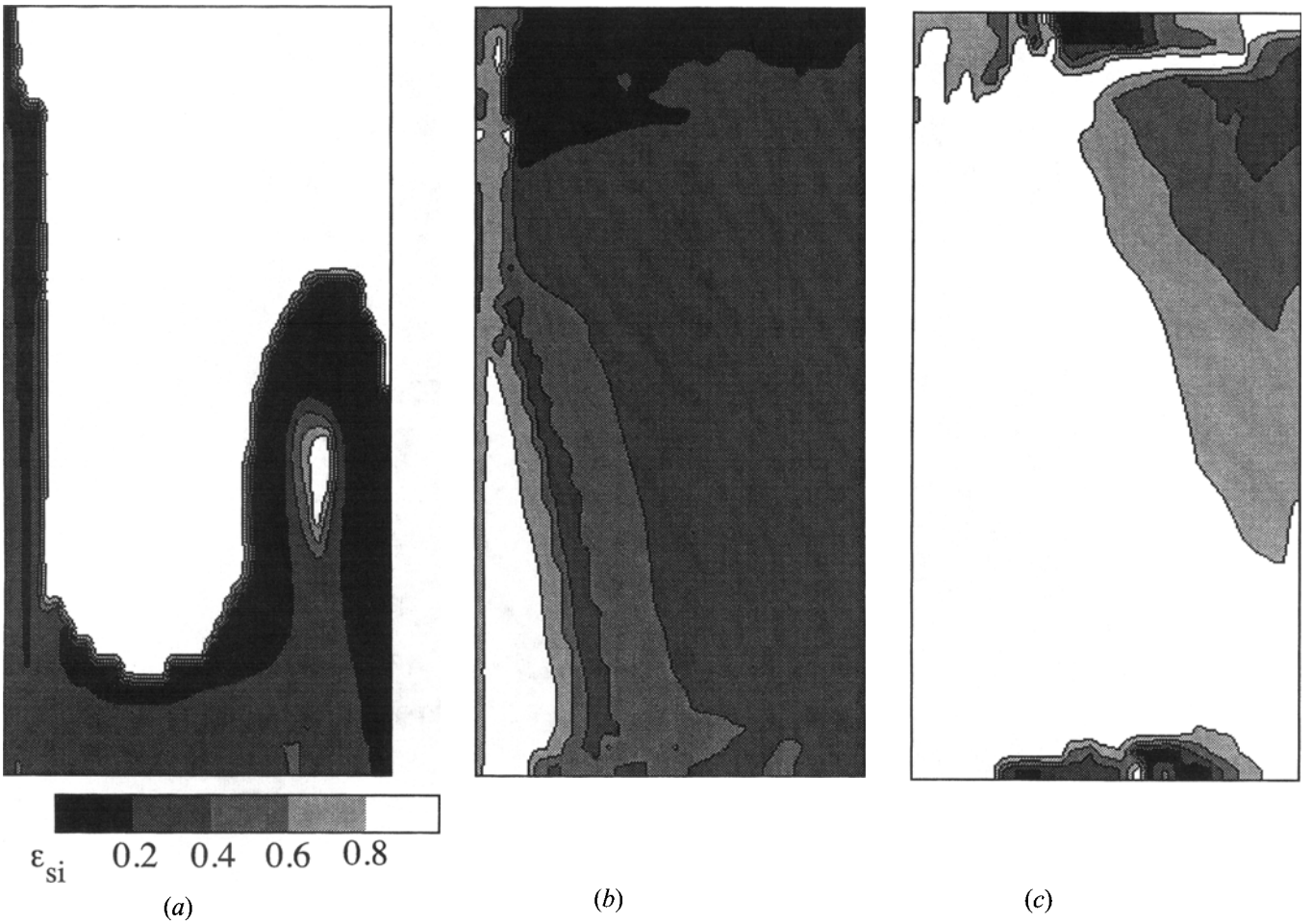

Fig. 15—Predicted internal solid fraction for case III at (*a*) t = 10 s, (*b*) t = 100 s, and (*c*) t = 250 s.

2. *Intermediate stages of solidification*

Simulation results at an intermediate stage of solidification are shown in Figure 11 for t = 150 seconds. Figure 11(a) shows that only a thin pure liquid layer exists in the upper right-hand corner. However, at the bottom of the cavity, a small region with a lower gray level can be observed, implying that the solid fraction there has decreased. The cause of this remelting phenomenon can be inferred from Figure 11(b), which shows a high copper concentration at the same location. Even after the formation of the packed bed, the solute-rich liquid continues to flow downward and collect at the bottom due to its high density. This liquid greatly depresses the liquidus temperature and even causes remelting of the solid that settled there at an earlier time. To provide direct evidence of remelting at the bottom, the predicted phase change rates are plotted in Figure 13 for t = 140 and 350 seconds. It can be seen from Figure 13(a) that indeed there is a pronounced remelting zone at the bottom at t = 140 seconds, leading to the decreased solid fraction observed at that location at t = 150 seconds (Figure 11(a)). Additional remelting pockets can be observed in the upper portion of the cavity.

The isotherms bend toward the right side on the bottom (Figure 11(c)). The relative velocity distribution shown in Figure 11(d) has a qualitatively similar pattern as before.

3. *Later stages of solidification*

At a later stage of solidification (t = 350 seconds, Figure 12), a lower solid fraction still can be observed at the bottom, despite the fact that this region has begun to resolidify (as shown by the predicted phase change rate in Figure 13(b)). The lower solid fraction is due to the prior remelting. In addition, the upper thin liquid layer has solidified appreciably. Overall, higher solid fractions prevail throughout the mushy zone, so that the liquid velocity is drastically reduced. The origin of the two white spots in the top-left corner of Figure 12(a) is presently not known.

The macrosegregation pattern shown in Figure 12(b) shows a considerable widening of the segregation zone in the left portion of the cavity where solidification is the fastest. The right half of the cavity is more positively segregated due to the advection of solute-rich liquid into this region. Another striking pattern is the bottom positive segregation, which is caused by the deposition of solute-rich liquid at the bottom, as discussed earlier.

Although the convection is weakened at this stage of solidification, the isotherms remain somewhat curved (Figure 12(c)). The relative velocity distribution shown in Figure 12(d) indicates no significant sedimentation of crystals occurring at this stage of solidification.

4. *Final macrosegregation and eutectic distribution*

The final macrosegregation pattern shown in Figure 6(b) for case III is very similar to the one at t = 350 seconds

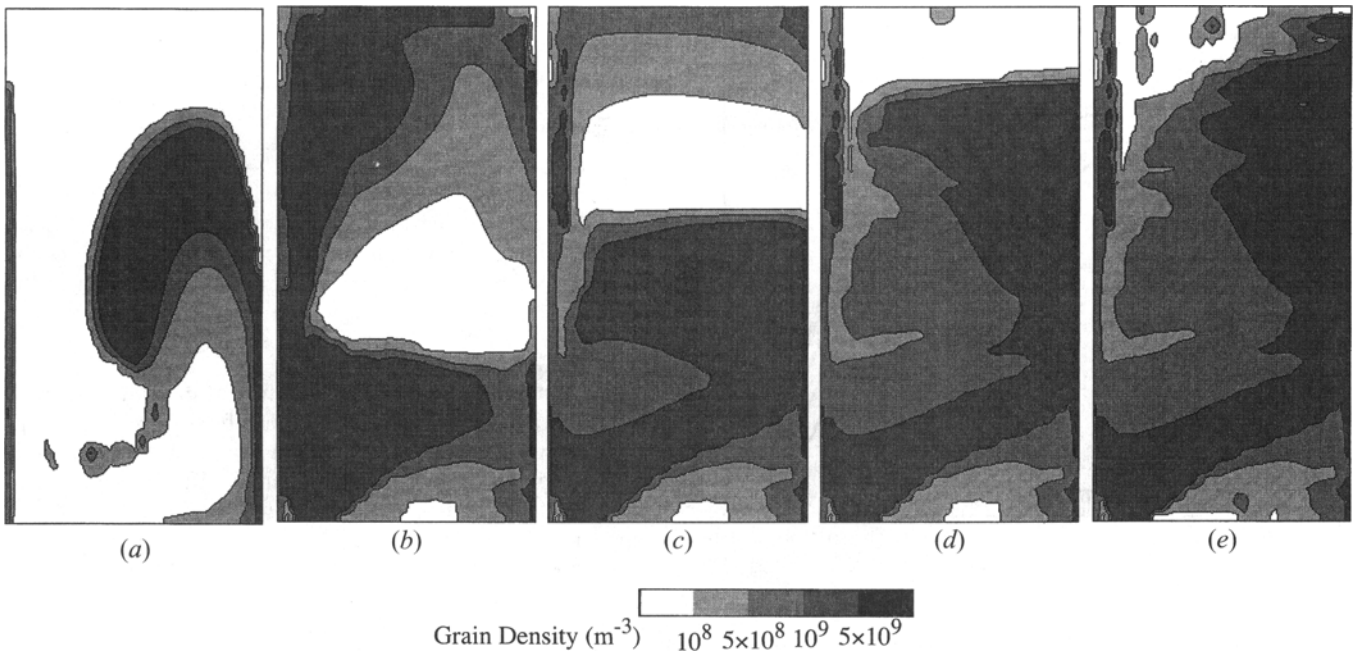

Fig. 16—Evolution of the grain density for case III at (*a*) t = 10 s, (*b*) t = 30 s, (*c*) t = 50 s, (*d*) t = 100 s, and (*e*) final.

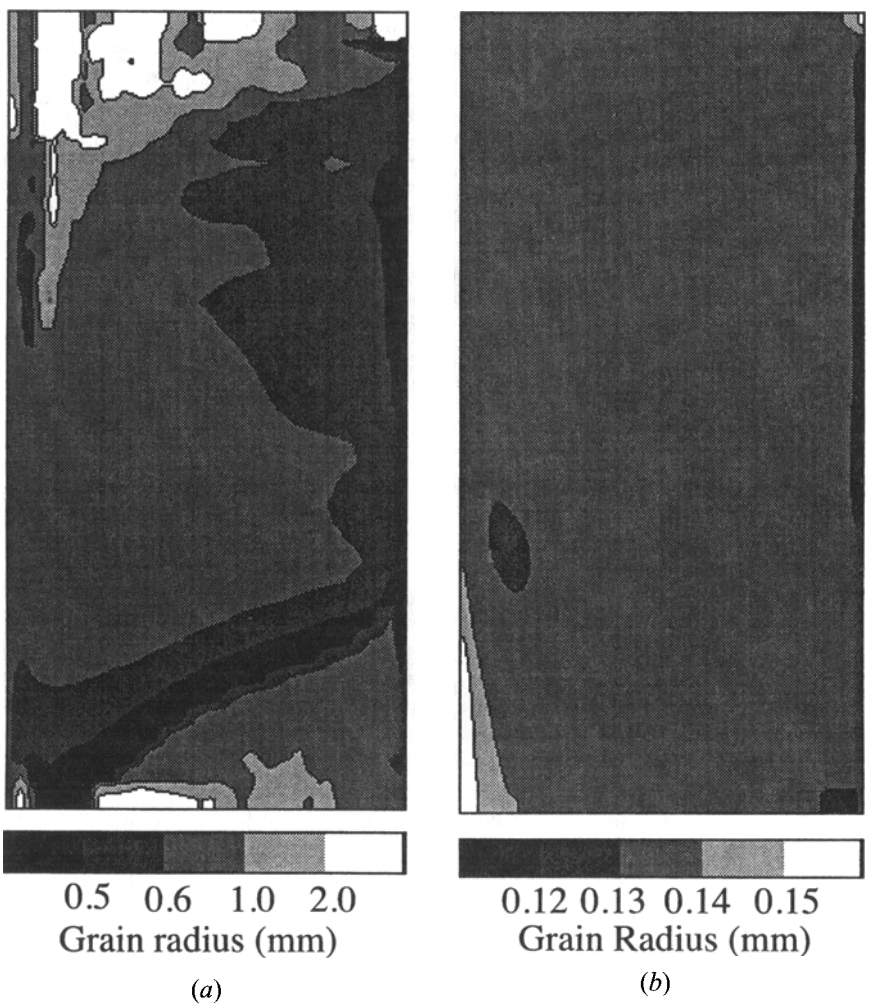

Fig. 17—Predicted final grain size (R_e) distribution for (*a*) case III: $n_0 = 10^9$ m^{-3}; and (*b*) case IV: $n_0 = 10^{11}$ m^{-3}.

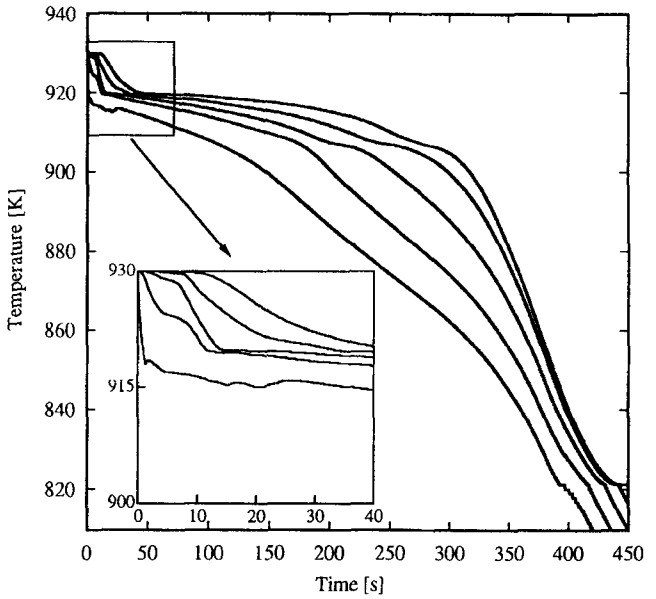

(*a*)

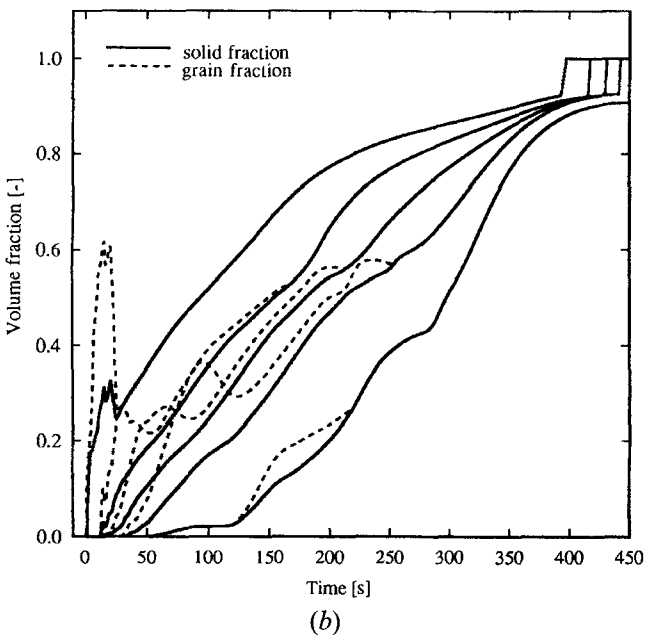

(*b*)

Fig. 18—(*a*) Cooling curves and (*b*) solid and grain fraction evolutions in equiaxed dendritic solidification with a high nucleation rate (case IV) for the same five interior locations as in Fig. 3.

(Figure 12(b)), indicating that there is no appreciable interdendritic liquid flow beyond $t = 350$ seconds. As compared to the macrosegregation pattern shown in Figure 6(a) for case II, the pattern for case III (Figure 6(b)) has several distinctive features. First, macrosegregation is less severe overall. This is because the solute-rich liquid and the solute-poor solid flow simultaneously downward. Hence, the macrosegregation due to relative phase motion is reduced. Second, no channel segregates are observed in case III. This can also be attributed to solid movement, since the nonuniformities in the solid fraction associated with such channels are readily equalized by the mobile crystals.

It should be cautioned, however, that solid movement does not always result in a more uniform composition on the system scale. Other alloy systems exist, in which the solute-rich liquid flows upward and the solid settles down, so that the solute-rich liquid will be separated from the solute-poor solid. This would cause very severe macrosegregation. More simulations should be conducted to capture these and other macrosegregation patterns (discussed further in part III).

Consistent with the macrosegregation pattern, the final eutectic fraction distribution displayed in Figure 14(a) for case III indicates a significant amount of eutectic at the bottom, whereas nearly no eutectic phase is present in the upper left corner.

5. *Microstructure*

The nature of the dendritic structure of the equiaxed crystals evolving during solidification can be deduced from Figure 15, where the internal solid fraction distribution is plotted for different times. Similar to diffusion-dominated solidification (Figure 4), highly dendritic structures always appear just behind the liquidus front where equiaxed crystals undergo free growth (Figure 15(a)). After the grains grow to a sufficiently large size, they impinge upon each other, whereas the dendrite arms keep thickening due to solidification. Therefore, the internal solid fraction is close to unity near the cold wall at $t = 100$ seconds (Figure 15(b)). At $t = 250$ seconds (Figure 15(c)), the relatively low internal solid fraction in the top and upper right portions of the cavity corresponds to the regions that solidify last, while the highly dendritic structure at the bottom coincides with the bottom remelt zone explained earlier.

Another interesting microstructural parameter is the grain density or, equivalently, grain size. In case III, the local grain density is not only determined by the nucleation rate but is also influenced by the solid motion during solidification. The advection of solid will cause a redistribution of the grains, in addition to influencing the nucleation process itself.

Figure 16 illustrates the evolution of the grain density. It can be seen from Figure 16(a) that a stream of highly concentrated nuclei is swept into the central part of the cavity. Notice that at this time (*i.e.*, $t = 10$ seconds), the solid motion is extremely strong due to the small size of the nuclei and the vigorous liquid flow. At $t = 30$ seconds (Figure 16(b)), the crystals lifted by the liquid flow along the right wall begin to resettle along the left wall. In addition, a central region of lower grain density appears. This is because the crystals in this region grew to such a large size that they settled down. The grains present in the upper region of the cavity, however, are too small to settle, so that the grain density remains high. This effect becomes more evident in Figure 16(c), which shows that the relatively sharp and horizontal interface between the regions of high and low grain densities coincides with the interface between the crystal sediment bed and the nearly solid-free liquid region (Figure 10(a)). At $t = 100$ seconds (Figure 16(d)), the zone of low grain density is shifted upward as the sediment bed increases in height.

The grain density ceases to evolve at about 350 seconds (Figure 16(e)). At this time, the nucleation process is completed throughout the domain and solid movement is absent as the grains impinge upon one another. The top zone of low grain density can be attributed to the sedimentation effect. In addition, it can be seen that a small region at the bottom appears where the grain density also is low. This is

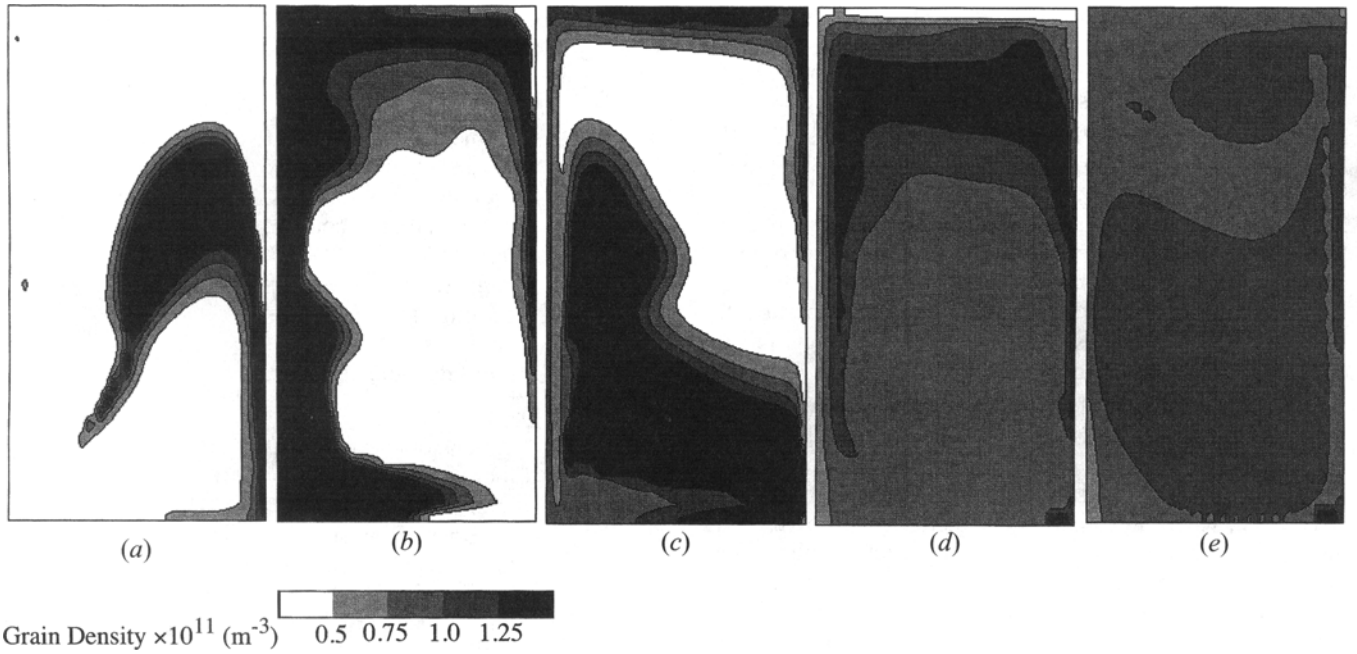

Fig. 19—Evolution of the grain density for case IV at (*a*) t = 10 s, (*b*) t = 30 s, (*c*) t = 50 s, (*d*) t = 150 s, and (*e*) final.

mainly caused by the remelting phenomenon explained earlier, which kills a number of grains in this region.

The corresponding final grain size distribution for case III is shown in Figure 17(a). Relatively fine grains of about 0.62 mm in size (*i.e.*, radius) are found mostly in the lower middle portion of the cavity. Crystals with a size larger than 2 mm are located at the top of the cavity due to crystal sedimentation as well as at the very bottom as a result of remelting.

D. *Case IV: Solidification with a High Nucleation Rate*

Based on case III, it is of interest to further explore the solidification and transport behaviors when the nucleation rate constant n_0 is raised from 10^9 to 10^{11} (m^{-3}). Two significant consequences are associated with higher nucleation rates and therefore smaller grains: (1) the equiaxed crystals tend to grow in a more globulitic fashion, and (2) there is less relative motion between the solid and liquid phases due to the larger interfacial drag.

The first consequence can be seen readily from Figure 18. The grain fractions at most internal locations evolve closely with the solid fractions, implying that the internal solid fraction is much closer to unity than in case II and III (compare Figures 18(b), 5(b), and 8(b)). This is a clear indication of more globulitic solidification, as may be expected in grain-refined castings. The oscillations in the solid and grain fractions for case IV are similar to case III, again because of solid motion. Another fact noticed in Figure 18(b) is that crystal impingement (where $\varepsilon_g = 0.637$) is significantly delayed in solidification with a high nucleation rate (case IV) when compared to solidification with a low nucleation rate (case III). This has a profound effect on the multiphase flow patterns during solidification. The recalescence shown in the inset of Figure 18(a) is also less pronounced than in Figures 5(a) and 8(a) for cases II and III, respectively.

The reduced slip velocity between the liquid and solid phases in case IV can be observed by comparing the magnitudes of the relative velocity. In case III, the difference between the solid and liquid velocities is of the order of 5 mm/s, whereas in case IV, this value is reduced to 1 mm/s. The lower settling velocity of the solid combined with the delayed packing in case IV promotes vigorous advection of the solid inside the cavity. Ultimately, this leads to much more homogeneous compositional and structural distributions in the final casting. Figure 6(c) demonstrates a relatively uniform final macrosegregation pattern, and Figure 14(b) accordingly shows a more uniform distribution of the eutectic phase. To help in understanding how a homogeneous grain size distribution results from the highly dispersed flow of the solid crystals, Figure 19 displays the evolution of the grain density in case IV. At t = 10 seconds (Figure 19(a)), a stream of high nuclei density, originating near the cold left wall, is circulating into the center of the cavity. This stream of nuclei is seen to descend along the left wall and arrive at the bottom at t = 30 seconds (Figure 19(b)). Because the small size of the crystals prevents their deposition at the bottom, the circulation of the solid inside the cavity continues (Figures 19(c) and (d)). At about t = 350 seconds (Figure 19(e)), the final grain density pattern is reached. The grain density throughout most of the cavity varies only over a narrow range (between 0.75 and 1.25 × 10^{11} m^{-3}). The corresponding final grain size distribution, therefore, is quite uniform over the entire cavity, as shown in Figure 17(b).

To sum up, this last simulation clearly identifies a multitude of important roles played by grain refiners: grain refining not only produces fine and uniform grain structures but also reduces the severity of the macrosegregation by promoting solid motion together with melt convection during most of the solidification process.

V. CONCLUSIONS

Using the multiphase model proposed in part I, a detailed numerical study was conducted for 2-D equiaxed dendritic

solidification of an Al-4 wt pct Cu alloy. The following main conclusions can be drawn from the present study.

1. Through comparisons among four different cases, it is shown how severe compositional and structural inhomogeneities in a casting can be caused by gravity-induced melt convection and solid movement.

2. As demonstrated in case II, channel segregates may arise from thermosolutal convection within a stationary mushy zone. In the Al-Cu alloy, the channels are oriented downward, as observed previously in laboratory experiments. This study also provides evidence that remelting is associated with the formation of channel segregates.

3. As shown in case III, solid movement reduces macrosegregation. This is because of the concurrent flow of solute-rich liquid and solute-poor solid in the present system. The effect of solid transport becomes even more obvious in case IV, where the small crystals closely follow the liquid flow. However, to fully assess the effect of solid transport on macrosegregation, future research is needed to study other alloy systems in which the solute-rich liquid tends to separate from the solute-poor solid (*i.e.*, countercurrent liquid-solid flow).

4. The predicted grain size distributions for cases III and IV clearly demonstrate that there exists no one-to-one correspondence between the nucleation rate and the local grain size whenever solid motion is present. Hence, the final grain size, which is routinely measured from micrographs of solidified materials, cannot be directly used to infer the nucleation rate, because the grain density distribution may be altered by flow during solidification. However, the knowledge of the measured final grain size, combined with the prediction of solid transport as shown in this study, would enable the development of a realistic nucleation model. Herein lies an important practical significance of the present numerical study.

5. Promotion of solid motion together with liquid flow is shown to provide an effective means of controlling the structure and chemical homogeneity of a casting. Although this is a well-known fact in practice, the present model simulations reveal for the first time the detailed transport mechanisms responsible for the formation of a variety of inhomogeneities. Nonetheless, thorough experimental validation is required before the model can be applied with confidence.

NOMENCLATURE

C	concentration of a chemical species, wt pct
c	specific heat, J/kg K
C_ε	settling ratio
d_e	mean characteristic diameter of the dendrite envelope, m
D	mass diffusion coefficient, m²/s
h	chill heat-transfer coefficient (W/m² K) or enthalpy (J/kg)
Iv	Ivantsov function
k	thermal conductivity, W/m K
l	species diffusion length, m
m_l	liquidus line slope, K/wt pct
$\mathbf{M}_s^d$	solid/liquid interfacial drag, N/m s
n	equiaxed nuclei density, m^{-3}
$\mathbf{n}$	outwardly directed unit normal vector
Pe_ε	multiphase Pelcet number, $\varepsilon_l\lvert\mathbf{v}_l - \mathbf{v}_s\rvert d_e/D_l$
Pe_t	solutal Peclet number at the dendrite tip, $V_t R_t/2D_l$
Pe_∞	ambient Pelcet number for dendrite tips, $\lvert\mathbf{v}_l - \mathbf{v}_s\rvert R_t/D_l$
R_t	tip radius, m
S	interfacial area concentration, m^{-1}
t	time, s
T	temperature, K
$\dot{T}$	cooling rate, $\partial T/\partial t$ (K/s)
$\mathbf{v}$	velocity vector, m/s
w	interface velocity, m/s

Greek Symbols

β	dimensionless parameter
γ	momentum dispersion coefficient
Γ	interfacial phase change rate (kg/m³ s) or Gibbs–Thomson coefficient (m K)
Δh	latent heat of phase change, J/kg
ε	volume fraction
ε_{si}	internal solid fraction, $\varepsilon_s/(\varepsilon_s + \varepsilon_d)$
κ	partition coefficient, wt pct/wt pct
κ_v	flow partition coefficient
λ_2	secondary dendrite arm spacing, m
λ_p	slip coefficient for solid, m
ρ	density, kg/m³
μ	viscosity, Pa s
σ^*	stability constant
Ψ	a field property
Ω	solutal supersaturation, $(\overline{C}_e - C_l)/[\overline{C}_e(1 - \kappa)]$

Subscripts

d	interdendritic liquid
e	dendrite envelope
E	eutectic point
eff	effective
f	total liquid phase ($d + l$)
g	grain
k	phase k
l	extradendritic liquid
L	liquidus
ld	extradendritic-interdendritic liquid interface
m	melting point of pure metals
n	normal direction
N	nucleation
0	initial state
s	solid
sd	solid-interdendritic liquid interface
t	dendrite tip or tangential
w	wall

Superscripts

c	critical
$-$	interfacial area-averaged
$*$	effective

ACKNOWLEDGMENTS

This work was supported by the National Aeronautics and Space Administration under Grant No. NCC3-290. The authors would like to thank Mr. C. Fan for his help with the numerical simulations.

REFERENCES

1. M. Rappaz: *Int. Mater. Rev.*, 1989, vol. 34, pp. 93-123.
2. Ph. Thévoz, J.L. Desbiolles, and M. Rappaz: *Metall. Trans. A*, 1989, vol. 20A, pp. 311-22.
3. J. Ni and C. Beckermann: *J. Mater. Processing Manufacturing Sci.*, 1993, vol. 2, pp. 217-31.
4. C.Y. Wang and C. Beckermann: *Metall. Mater. Trans. A*, 1995, vol. 27A, pp. 0000-00.
5. W. Kurz and D.J. Fisher: *Fundamentals of Solidification*, Trans Tech Publications, Aedermannsdorf, Switzerland, 1989, p. 91.
6. C.Y. Wang, S. Ahuja, C. Beckermann, and H.C. de Groh III: *Metall. Mater. Trans. B*, 1995, vol. 26B, pp. 111-19.
7. J. Ding and D. Gidaspow: *AIChE J.*, 1990, vol. 36, pp. 523-38.
8. D.M. Stefanescu, G. Upadhya, and D. Bandyopahyoy: *Metall. Trans. A*, 1990, vol. 21A, pp. 997-1005.
9. R. Ananth and W.N. Gill: *J. Crystal Growth*, 1991, vol. 108, pp. 173-89.
10. C.Y. Wang: Ph.D. Thesis, The University of Iowa, Iowa City, A, 1994.
11. S. Ganesan and D.R. Poirier: *Metall. Trans. A*, 1987, vol. 18A, pp. 721-23.
12. S.V. Patankar: *Numerical Heat Transfer and Fluid Flow*, Hemisphere Publishing Corp., New York, NY, 1980.
13. D.B. Spalding: in *Recent Advances in Numerical Methods in Fluids*, C. Taylor and K. Morgan, eds., Pineridge Press, Swansea, 1981, vol. 1, pp. 139-67.
14. M. Rappaz and Ph. Thévoz: *Acta Metall.*, 1987, vol. 35, pp. 1487-97.
15. C.Y. Wang and C. Beckermann: in *Materials Processing in the Computer Age II*, V.R. Voller, S.P. Marsh, and N. El-Kaddah, eds., TMS, Warrendale, PA, 1995, pp. 129-43.
16. V.R. Voller: *Numerical Heat Transfer*, 1990, vol. 17, pp. 155-69.
17. R. Mehrabian, M.A. Keane, and M.C. Flemings: *Metall. Trans.*, 1970, vol. 1, pp. 3238-41.
18. W.D. Bennon and F.P. Incropera: *Metall. Trans. B*, 1987, vol. 18B, pp. 611-16.
19. S.D. Felicelli, J.C. Heinrich, and D.R. Poirier: *Metall. Trans. B*, 1991, vol. 22B, pp. 847-59.
20. M.C. Schneider and C. Beckermann: *Int. J. Heat Mass Transfer*, 1995, in press.
21. L.H. Shaw, J. Beech, and R.H. Hickley: *Ironmaking and Steelmaking*, 1986, vol. 3, pp. 154-60.
22. A. Hellawell, J.R. Sarazin, and R.S. Stuebe: *Phil. Trans. R. Soc. Lond. A*, 1993, vol. 345, pp. 507-44.
23. H. Jones: *Mater. Sci. Eng.*, 1984, vol. 65, pp. 145-56.